Gas gun driven dynamic expansion of 3D-printed AlSi10Mg rings

J. C. Nieto-Fuentes[a,*], T. Virazels[a], N. Jacques[b], J. A. Rodríguez-Martínez[a]

[a]*Department of Continuum Mechanics and Structural Analysis. University Carlos III of Madrid. Avda. de la Universidad, 30. 28911 Leganés, Madrid, Spain*

[b]*ENSTA Bretagne, CNRS UMR 6027, IRDL, 2 rue François Verny, F-29806 Brest Cedex 9, France*

Abstract

This paper presents a new experimental setup to study dynamic fragmentation of metallic rings manufactured by 3D-printing technology. The ring is inserted over a ductile thin-walled tube which is impacted axially by a conical-nosed cylindrical projectile fired by a single-stage light-gas gun. The diameter of the projectile is larger than the internal diameter of the thin-walled tube, which expands as the projectile advances, pushing radially outwards the metallic ring, that eventually breaks into multiple fragments. The impact velocities considered in the present experimental campaign range from 197 m/s to 385 m/s. The AlSi10Mg ring specimens are printed by Selective Laser Melting technique, with an inner diameter of 14 mm and square cross section of 2×2 mm^2. To obtain time-resolved information on the mechanics of fragmentation, the number of fractures, and the size of the fragments, the tests have been recorded with two-high speed cameras. A tunnel-shaped soft casing made of polymer foam is placed around the specimen to softly recover the ejected fragments, that have been weighted and sized to determine the statistics of the fragments size distribution. In addition, the predictions of the fragmentation theory of Kipp and Grady [12] for the evolution of the number of fragments with the impact velocity have been compared with the experimental evidence, and an excellent quantitative agreement has been found within the whole range of loading rates investigated. Compared to other available techniques for dynamic fragmentation of rings, in which the expansion of the specimen is driven by electromagnetic or explosive loading, this experimental setup stands out for its simplicity, fast operation, quick assembly, and flexibility to test different engineering materials, which facilitates performing extensive experimental campaigns (34 successful tests have been carried out in this research). To the authors' knowledge, this paper presents the most comprehensive data set to date on the fragmentation of dynamically expanded printed rings, including the first high-resolution video recordings of the formation of multiple cracks throughout the circumference of the samples, and scanning electron microscopy images of the fractures showing the porous microstructure on the cracks surface.

Keywords:

Ring expansion, High-speed impact, Dynamic fragmentation, Additively-manufactured metals

*Corresponding author. Tel. +34 916249588, E-mail address: junietof@ing.uc3m.es

1. Introduction

The ring expansion test devised by Niordson [20] was a turning point in the experimental investigation of material behavior at high strain rates. An electromagnetic loading scheme was used to expand copper and aluminum rings at radial velocities ranging from 40 m/s to 400 m/s. The testing setup consists of a condenser battery discharged into a coil over which the ring is inserted. The coil creates an electromagnetic-field induced current in the ring which interacts with the primary current flowing in the coil, generating repulsive forces between the ring and the coil, leading to a rapid expansion of the specimen. This experimental technique is particularly suitable to test materials which are good electrical conductors. However, the induced current in the ring results in Joule heating effects that significantly increase the temperature of the specimen (note that Cliche and Ravi-Chandar [2] estimated the increase of temperature due to Joule effect in dynamically expanded AZ31B-O rings to be more than 200 K (see Fig. 6c therein)). The inner diameter of the rings tested by Niordson [20] was 140 mm, with axial thickness of 10 mm and radial thickness of 1 mm, so that the radial stress was negligible in comparison with the circumferential stress, and the stress field was mainly uniaxial. The highest strain rate attained in these tests, approximately 5700 s^{-1}, was several times greater than in a conventional Split Hopkinson Tension bar experiment. A salient feature of the electromagnetic loading scheme is that the loading rate is readily controlled through the variation in frequency and intensity of the primary current pulse. Moreover, the radial symmetry of both specimen and loading minimizes the intervention of stress waves along the circumferential direction of the specimen, so that the ring shows practically uniform strain field until deformation is not longer homogeneous at large strains, leading to plastic localization and multiple fractures.

Some years later, Fyfe and Rajendran [4], and Rajendran and Fyfe [22], designed an alternative system to dynamically expand metal rings, which consisted of an exploding wire placed along the axis of a polyethylene hollow cylinder over which the specimen was fitted. Wire vaporization, occurring due to the energy released from high-voltage capacitors, generates a wave disturbance that propagates through the medium surrounding the wire to impinge uniformly on the inner wall of the cylinder, hence inducing an uniform radial cylindrical stress wave into the ring. The tests were performed using aluminum 6061-T6 and annealed copper specimens with internal diameter of 25.4 mm, width of 3 mm, and different thicknesses ranging from 0.5 mm to 1.0 mm. The experiments were conducted at various voltage levels of the capacitor bank, so that increasing the energy release increased the loading rate in the specimen and thus the number of pieces into which the ring broke. For the highest strain rate levels, up to 10 fractures were observed. Moreover, Grady and Benson [6] implemented similar electromagnetic experimental arrangement to Niordson [20] and tested OFHC copper and aluminum 1100–O rings to radial velocities up to 200 m/s. The samples had a 32 mm inner diameter and a square cross section of 1 mm^2, such that the maximum circumferential strain rate attained in the rings was approximately 10^4 s^{-1} (roughly double than in Niordson [20] setup, because the samples tested had a smaller diameter). The time resolved motion of the ring-shaped specimens was recorded with a streak-camera technique, verifying that the expansion process was uniform and stable, with an initial acceleration region followed by an interval of nearly constant velocity, when the nucleation of multiple necks and fractures led to the fragmentation of the samples. Not all the necks developed into fractures. Here, arrested necks are presumed to result from the arrival of a relief stress wave from a nearby fracture that removes the driving force before fracture completion. The fragments were recovered, determining the number and size distributions. The number of fragments and the fracture strain were shown to increase with the expansion velocity for both aluminum and copper samples.

Altynova et al. [1] performed electromagnetic ring expansion experiments with aluminum 6061 and OFHC copper samples, for radial speeds ranging between 50 m/s and 300 m/s. The ring-shaped specimens had inner and outer diameters of 30.5 mm and 32.5 mm, respectively, and different widths varying from 1 mm to 2 mm. Consistent with the results of Grady and Benson [6], the number of necks, the number of fragments and the fracture strain were shown to increase with the expanding velocity. For instance, at an expansion velocity above 200 m/s, the dynamic ductility of aluminum 6061 and OFHC copper rings exceeded the quasi-static value by 60% and 250%, respectively. The improved ductility at large expanding velocities was attributed to inertia effects at high strain rates. Dynamic fragmentation experiments on rings of U6N were carried out by Grady and Olsen [8]. The samples with 30 mm of inner diameter were tested at expansion velocities within the range $50 - 300$ m/s. The number of fragments, the distributions in fracture spacing and fragment masses, and the strain to fracture were compared with the statistical-based fragmentation theory of Mott [18] and with the energy-based fragmentation theory of Kipp and Grady [12]. These theories postulate that fragmentation of metals under intense tensile impulsive loading occurs due to the activation of material weak points which are scattered throughout the sample (material defects such as pores, cavities and cracks formed during material processing) and determine the distribution of fracture points. The predictions obtained with both theoretical approaches agreed reasonably well with the experimental data that, similarly to the results of Grady and Benson [6], and Altynova et al. [1], for copper and aluminum specimens, showed an increase in the number of fractures and in the fracture strain with the expansion velocity.

Shortly after the paper of Grady and Olsen [8], Zhang and Ravi-Chandar [30] presented the first implementation of the electromagnetic loading scheme of Niordson [20] in which high-resolution, high-speed images of the ring expansion process were acquired showing the formation of multiple necks and fractures. Aluminum 6061-O specimens with inner diameter of 30.5 mm, and rectangular cross section of thickness 0.5 mm and length 1 mm, were tested at velocities ranging from 80 to 200 m/s. Following Mott [18] postulates, the distribution of neck spacings and fragment sizes was attributed to the spatial variability of the necking and fracture strains throughout the circumference of the ring, and to the unloading waves released from growing necks and early fractures. It was concluded that the release wave mechanism sets the scale for fragmentation, so that the decrease in the necks spacing and in the fragments size with the increase of the expansion velocity occurs because the unloading engendered by any localization and fracture does not travel far enough quickly to inhibit further localization and fracture at neighboring locations. In a companion paper, Zhang and Ravi-Chandar [31] carried out additional ring expansion experiments with Al 1100-H14 and Cu 101 specimens for expansion velocities ranging from 65 to 230 m/s. The tests resulted in statistical distributions of neck spacings and fracture sizes similar to those obtained in the experiments with Al 6061-O rings in Zhang and Ravi-Chandar [30], such that with increasing strain rate, more necks and fractures were nucleated at shorter distances. The same experimental setup was used years later by Cliche and Ravi-Chandar [2] to investigate the fragmentation behavior of annealed AZ31B-O magnesium alloy. Experiments in which the electromagnetic-field induced current circulates in the magnesium specimen were compared with tests in which a copper pusher ring is used to carry the induced current, in order to reduce the Joule heating effects in the magnesium specimen. Samples with inner diameter of 31.5 mm, length of 0.5 mm, and two different thicknesses of 0.5 mm and 2.286 mm were tested at expanding velocities ranging from 40 m/s to 200 m/s. The experiments did not reveal any measurable effect of the expansion velocity and the Joule heating on the ductility of the magnesium rings, suggesting that the onset of necking localization in AZ31B-O is not affected by thermal softening for temperatures below half of the melting point. On the other hand, the increase of the cross section of the specimen boosted the strain developed in the unnecked regions of the ring, probably due to enhanced inertia effects with the increase of the specimen size (inertia increases with the thickness of the sample). Fragmentation behavior of magnesium was also investigated by Kahana et al. [11] expanding AZ31 ring-shaped specimens at strain rates ranging from $6 \cdot 10^3$ s^{-1} to $1.2 \cdot 10^4$ s^{-1}. The dimensions of the specimens were 36 mm of outer diameter, 32.6 mm of inner diameter, and 2.4 mm of width. The fracture strain of the material increased with the strain rate from 0.18 to 0.34, while the sum of necks and fractures raised from 2 to 21. Consistent with the results of Grady and Benson [6] and Altynova et al. [1] for copper and aluminum samples, these experiments indicated the increased ductility of AZ31 magnesium alloy at high strain rates (these results stand in contrast with the tests of Cliche and Ravi-Chandar [2] on AZ31B-O rings, which did not show a correlation between the necking strain and the strain rate).

Ring expansion tests on cold-rolled Cu-ETP copper, aluminum alloy 7075, barrel steel and tungsten heavy alloy were performed by Janiszewski [9] using a similar experimental setup to Grady and Benson [6]. While in the tests with copper and aluminum rings the induced current was beared by the specimen, in the experiments with barrel steel and tungsten alloy an indirect expansion technique using a copper pusher ring was employed to reduce the specimen heating resulting from the high current flow. All the specimens tested had a square cross-sectional area of 1×1 mm^2, the mean diameter being 32 mm for Cu-ETP copper and aluminum alloy 7075, 33.4 mm for barrel steel, and 27.2 mm for tungsten heavy alloy. The experiments, performed for expansion velocities ranging between 65 m/s and 275 m/s, showed the fracture strain to increase monotonically with the loading rate for Cu-ETP copper, barrel steel and tungsten alloy, while in the case of aluminum alloy 7075 the maximum ductility of the specimen corresponded to an intermediate value of the expansion velocity. Very recently, Wood et al. [29] performed electromagnetic ring expansion tests on Inconel 718 specimens fabricated using Laser Melting Powder Bed Fusion technique. A pusher ring made of copper was used to carry the induced current and expand the specimens at strain rates ranging from $8 \cdot 10^3$ s^{-1} at the peak radial velocity to $1.5 \cdot 10^3$ s^{-1} at fracture. The dimensions of the rings were 33.6 mm of outer diameter, 0.7 mm of wall thickness and 1 mm of length. The initial void volume fraction of the specimens was estimated using an empirical model which related the printing parameters with the residual porosity, so that the ring expansion tests suggested that increasing the material porosity drops the specimen ductility and increases the number of fragments. Moreover, it was concluded that the increase of the fracture strain with the strain rate is more important as the initial void volume fraction decreases. Electromagnetic ring expansion tests on aluminum alloy 5052 specimens were performed by Ma et al. [14]. The rings had an inner diameter of 65 mm and a square cross section of 1 mm^2, and were expanded at radial velocities varying from 60 m/s to 140 m/s, so that the strain rates ranged between 1800 s^{-1} and 3300 s^{-1}. The experiments were recorded with a high-speed camera, showing the formation of multiple necks evenly distributed around the circumference of the specimen, some of these necks ultimately developing into fractures. The number of necks and fragments was shown to increase with the strain rate, so that for the highest radial expansion velocity tested the number of fragments and necks amounted to 9 and 44, respectively.

An alternative to performing ring fragmentation tests using electromagnetic loading schemes is employing gas guns. Mechanical loading systems are generally more conducive to a laboratory environment, as they do not require the employment of large currents – up to 20 kA are needed to accelerate samples with sub-millimeter wall thickness to 200 m/s – and do not have the problem of the specimen being affected by Joule heating effects. Note also that extending the electromagnetic loading technique to larger specimens requires more current, and with higher currents the resistive heating thermally softens or even partially melts the sample, imposing a limitation to the range of sample sizes that can be tested with this technique [10]. Moreover, as inertia effects are proportional to the sample thickness squared [32], there is a need for testing larger samples to obtain further insights into the effect of inertia on dynamic fragmentation. Note that once inertia starts to play a role, the fragmentation mechanics depend on both material behaviour and specimen size (the fragmentation is no longer characteristic of a specimen but a structure). Stepanov and Babutskii [24] used a pneumatic solid fuel impact machine to investigate the fragmentation of metal rings subjected to dynamic expansion at radial velocities up to 500 m/s. Two different configurations were developed. In the first arrangement, the pneumatic impact machine was used to launch a conical projectile which penetrates axially the ring, the inner diameter of the specimen being smaller than the diameter of the base of the conical striker, so that the ring expands during the impact and ultimately breaks into pieces. In the second configuration, the ring is launched onto the striker, which is fixed. Note that the limitation in size of the specimens is that the diameter of the rings has to be smaller than the diameter of the gun barrel bore. Ring samples of different hardnesses (97 HV and 195 HV) with an outer diameter of 80 and 64 mm and a wall thickness of 4 and 3 mm, respectively, were tested. The experimental results showed that the number of fragments increases with increasing deformation velocity (consistent with all previous works cited in this introduction), and that the material with greater hardness breaks into a larger number of fragments. Gant et al. [5] developed a new experimental setup using a single-stage gas gun to study the fragmentation of metallic rings under dynamic radial expansion. The test consists of launching a steel ogival-nosed projectile onto a high-density polyethylene disk which is crushed onto a steel anvil, deforming and imparting radial momentum to a metal ring which expands at high strain rate and ultimately breaks into pieces. The ejected fragments were collected with a polymer foam casing surrounding the specimen. The rings tested had 40 mm of diameter and 1 mm^2 of square cross section. The experiments were performed using mild steel and aluminum alloy specimens, and recorded with a high-speed camera. The impact velocity of the projectile and the expansion velocity of the ring were measured with Photon Doppler Velocimetry probes. It was shown that for a given projectile velocity of 150 m/s, the maximum radial velocity of the aluminum rings is 40% larger, while the mild steel specimens show less number of fragments and greater strain at fracture. Note that similar experimental arrangements to Stepanov and Babutskii [24] and Gant et al. [5] were used by Winter and Prestidge [28], Vogler et al. [26] and Jones et al. [10], among others, to study dynamic fragmentation of metallic thin-walled cylinders.

In this paper, guided by the works cited in previous paragraph, we have developed and demonstrated a novel experiment which consists of an additively-manufactured ring specimen inserted over the edge of a ductile thin-walled tube (also referred to as hollow cylinder or pusher along this paper) which is impacted axially by a conical-nosed cylindrical projectile (also referred to as striker along this paper) fired by a single-stage gas gun. The cylindrical part of the projectile has a diameter approximately double than the inner diameter of the thin-walled tube, which expands as the projectile moves forward, pushing radially outward the metal ring, which ultimately breaks into multiple fragments. Compared to electromagnetic loading schemes, this experiment is a simple setup, which is fast to operate and assemble, and thus it is suitable to perform extensive experimental campaigns. The main practical limitation is that the inner diameter of the ductile hollow cylinder used as a pusher has to be smaller than the bore of the gun barrel. To the authors' knowledge, this paper presents the more comprehensive data set to date on the fragmentation of dynamically expanded printed rings.

2. Experimental setup

The experimental setup adapts the configuration recently developed by Nieto-Fuentes et al. [19] for the axial penetration of thin-walled cylinders to perform ring expansion tests. The actual setup is shown in Figures 1 and 2, with arrows and numbers indicating the main items of the setting, while the schematic of Fig. 3 shows the principle of operation of the experiment. The AlSi10Mg ring specimens were additively-manufactured by the company Materialise [15] by Selective Laser Melting (SLM) using two printing qualities, *standard* and *performance*, with nominal porosity of 3% and 0.5% [15], respectively. However, note that the tomography analysis performed by Nieto-Fuentes et al. [19] with as-printed thin-walled cylinders revealed that the porosity is actually larger, up to 6% and 2%, respectively. The experiments of Nieto-Fuentes et al. [19] —see Fig. 7 therein— also showed that the voids are largely spherical, with 90% of the pores having diameter smaller than 20 µm for both *standard* and *performance* samples. Moreover, the *standard* samples were shown to have 4% of the voids with diameter greater than 50 µm, while this percentage decreases down to 1.5% in the case of the *performance* specimens. The largest pores were located near the surface of the samples. The average surface roughness of the rings provided by Materialise [15] for *standard* and *performance* samples was $R_a = 10.75$ µm and $R_a = 7.0$ µm. These values are very similar to in-house experimental measurements obtained with an optical profilometer ZETA 20 3D. The rings tested in this paper have an outer diameter of 18 mm and a square cross section of 2×2 mm^2. We are aware that for these specimen dimensions, the effect of curvature in the deformation behavior of the ring may not be negligible [17]. On the other hand, we have performed finite element calculations showing that the stress and strain fields in the ring are rather uniform during the expansion (the results are not included in the paper for the sake of brevity). The pusher is made of AISI 316L steel, having an initial length of 40 mm, inner diameter of 14 mm and thickness of 2 mm. Note that AISI 316L steel is significantly more ductile than the additively-printed materials so that the first failure of the pusher occurs after the complete fragmentation of the ring specimens. A thin layer of grease is inserted between the ring and the pusher to reduce friction effects during the tests. The opposite end of the pusher to which the ring is mounted is inserted into a pyramidal support printed out of polylactide (PLA) thermoplastic polyester. The pyramidal support has 8 thin petals that embrace the pusher, extending until the rear part of the ring, so that the specimen does not move axially due to the air flow coming from the gas gun that precedes the arrival of the projectile. The pyramidal support sits on a XYZ assembly which integrates an XY precision table with a height regulator jack in order to ensure the alignment of the cylindrical specimen with the gun barrel before testing, so that the striker impacts uniformly on the inner perimeter of the pusher, and the ring expands radially. The XYZ assembly is screwed to an aluminium structure which is fixed to the laboratory floor (see Fig. 1), such that the position of the pyramidal support which holds the hollow cylinder is the same in all tests. Fine-tuning of the projectile trajectory is carried out using a laser that is passed through the gun barrel and the axis of the hollow cylinder before the experiment. However, for $\approx 20\%$ of the impact experiments performed, the flight of the projectile slightly deviated from a straight trajectory, with the first contact between projectile and pusher occurring on one side of the thin-walled tube. The tests in which the impact deviation was greater than 0.2 mm were discarded from the present test series (i.e., they are not included in Table 1). The striker was made out of quenched and tempered 42CrMo4 alloy, and it is 64 mm long, with a 1.55 mm nose radius, 40° apex angle, and a 24 mm diameter base (see Figure 2 in Nieto-Fuentes et al. [19]). A cup-type cylindrical sabot of 24.5 mm diameter and 100 mm long, printed out of PLA thermoplastic polyester, was inserted in a 20 mm long and 10 mm diameter pin machined at the projectile base (see Figure 2 in Nieto-Fuentes et al. [19]). The total mass of the assembly striker/sabot is 157 g.

The experiments have been performed at 4 different impact velocity ranges: 197 m/s $\leq v_z \leq$ 218 m/s, 246 m/s $\leq v_z \leq$ 259 m/s, 317 m/s $\leq v_z \leq$ 338 m/s and 363 m/s $\leq v_z \leq$ 385 m/s. The 25-mm bore barrel gas gun (manufactured by *Thiot Ingenierie*) was driven by helium, with the firing pressure in the reservoir being $P = 22$ bar and 95 bar for the lowest and highest impact velocity tested, respectively. The radial expansion velocity of the ring is computed as $v_r = \frac{v_z \sin(2\alpha)}{2}$, under the assumption that the pusher and the ring move perpendicular to the conical-nose of the projectile. Note that $\alpha = 70^{\circ}$ is the angle formed between the perpendicular and axial directions of the striker cone (see Figure 2 in Nieto-Fuentes et al. [19]). The nominal circumferential strain rate in the specimen $\dot{\varepsilon}_{\theta}$, computed as the radial expansion velocity over the initial inner radius of the ring, varies between 8000 s^{-1} and 15000 s^{-1} (similar range of strain rates was attained by Kahana et al. [11] using the electromagnetic expansion method, see Section 1). The tests have been recorded with two-high speed cameras Photron Fastcam SA-Z 2100K, using a frame rate of 200000 fps, a resolution of 256 px $\times$ 232 px, and a shutter speed of 1/2880000 s. Two lampheads provided the lighting required to film the experiments, the video recordings giving time-resolved information on the mechanics of fragmentation, the number of fractures and the size of the fragments (see Section 3). The impact velocity has been also measured using the video footage of the high-speed cameras which were calibrated before each test by setting a reference length to determine the pixel size, which allowed computing the distance traveled by the projectile within a given time interval (and thus obtaining the impact velocity). A tunnel-shaped aluminum casing lined with a polymer foam has been placed around the specimen to trap the ejected fragments, that have been weighted and sized to determine the statistics of the fragments size distribution. The fracture surfaces of selected fragments have been analyzed using scanning electron microscopy (SEM) in order to obtain information on the failure mechanisms and the porous microstructure of the specimens.

3. Results

This section presents the main results of the impact experimental campaign, including high-resolution snapshots of the fragmentation process, post-mortem analysis of fragment sizes, and scanning electron microscopy images of fracture surfaces. The dynamic fragmentation campaign comprises 34 successful experiments, out of which 19 correspond to specimens printed with quality *standard*, which are designated by Ring-Alu-S-1, ..., Ring-Alu-S-20, and the remainder correspond to samples with quality *performance*, which are referred to as Ring-Alu-P-1, ..., Ring-Alu-P-17 (note that results for samples Ring-Alu-S-19, Ring-Alu-P-9 and Ring-Alu-P-14 were discarded, as the striker did not impact axially on the hollow cylinder based on the standard established in Section 2). Section 3.1 compares two tests performed at similar impact velocity on *standard* and *performance* specimens to identify the mechanisms of fragmentation of the rings, and Section 3.2 investigates the influence of impact velocity on the number and the size distribution of the fragments, and compares the results with the predictions of the theory of

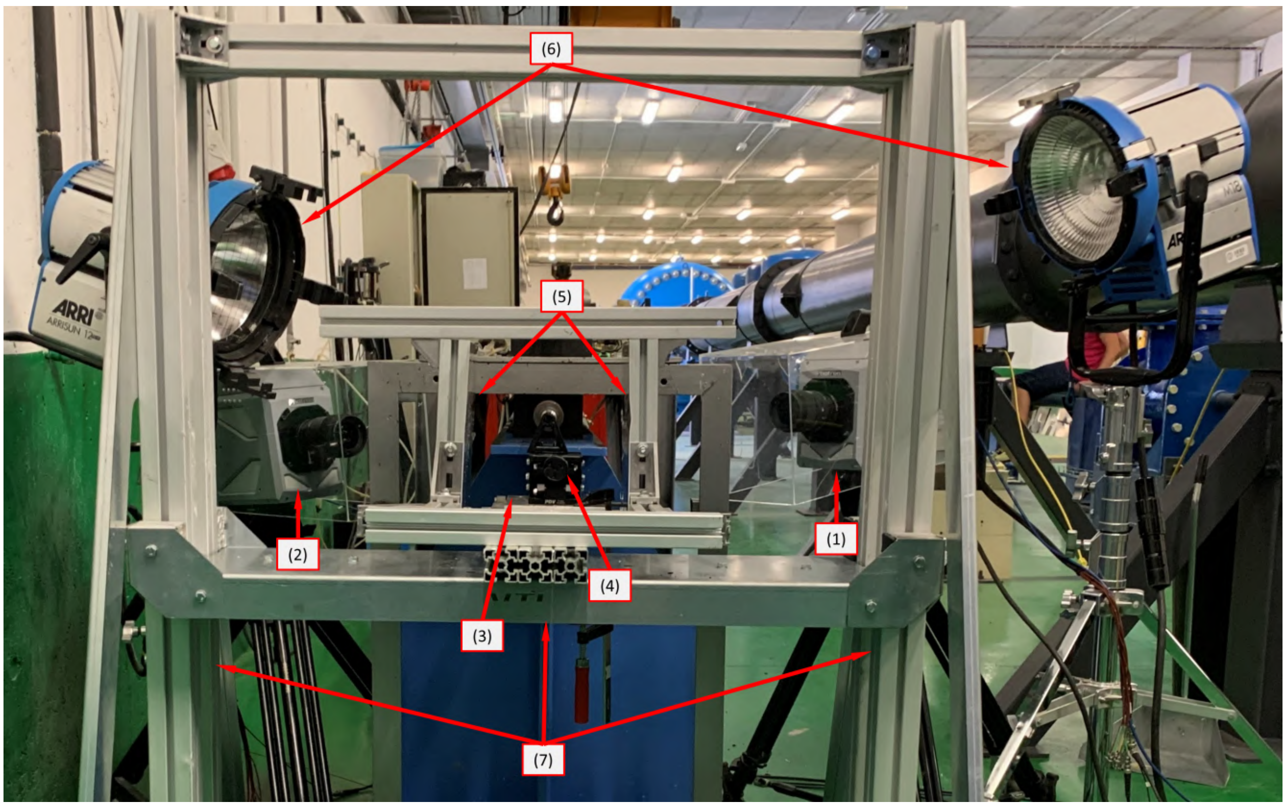

Figure 1: Experimental setup: (1) high-speed camera 1, (2) high-speed camera 2, (3) XY precision table, (4) height regulator jack, (5) tunnel-shaped aluminum casing (the foam has been removed to lighten the picture), (6) lampheads and (7) aluminium structure screwed to the laboratory floor.

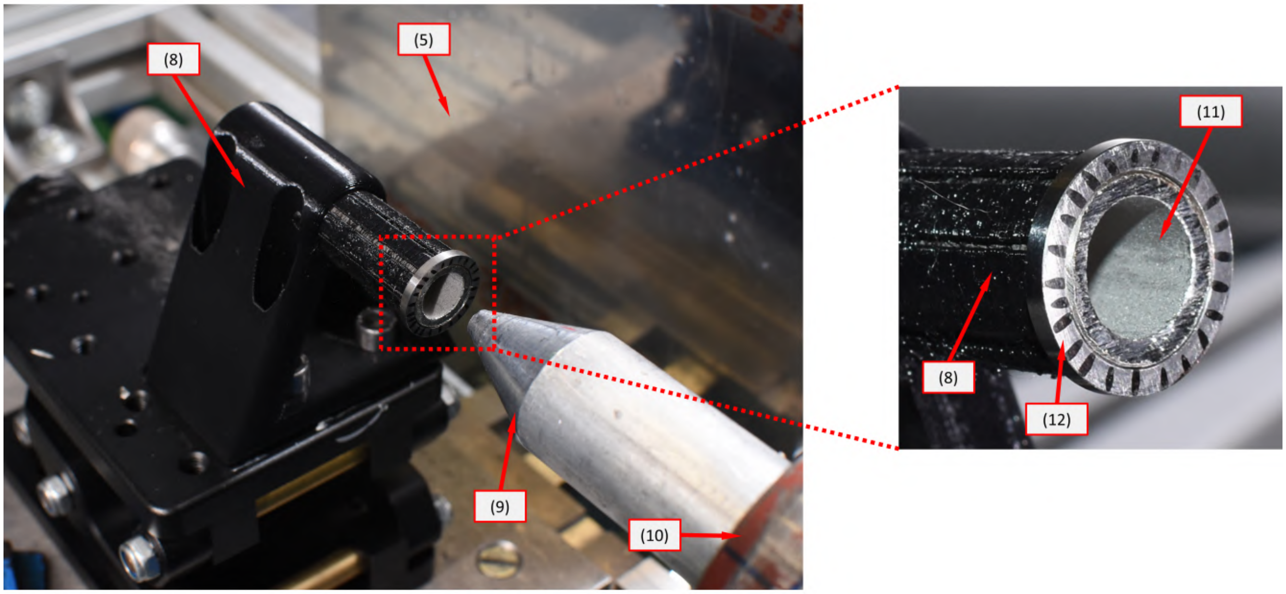

Figure 2: Experimental setup: (5) tunnel-shaped aluminum casing (the foam has been removed to lighten the picture), (8) pyramidal support, (9) conical-nosed cylindrical projectile, (10) gun barrel, (11) pusher and (12) ring specimen.

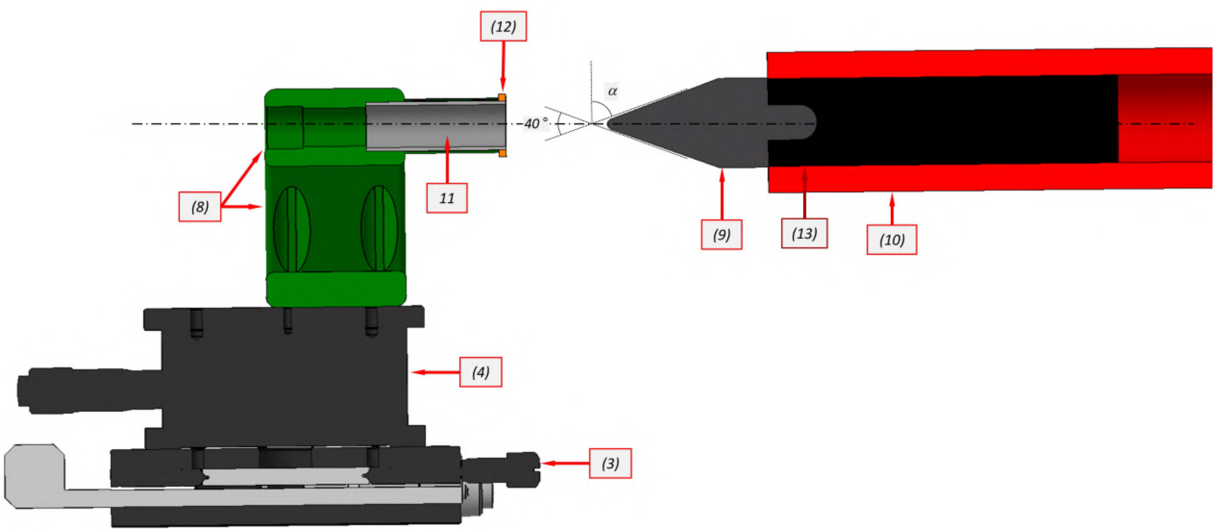

Figure 3: Schematic of the setup showing the principle of operation of the experiment. The ring is inserted over a thin-walled tube which is impacted axially by a conical-nosed cylindrical projectile fired by a single-stage gas gun. The diameter of the projectile is larger than the internal diameter of the thin-walled tube, which expands as the projectile advances, pushing radially outwards the metallic ring, that eventually breaks into multiple fragments. Main items of the setting: (3) XY precision table, (4) height regulator jack, (8) pyramidal support, (9) conical-nosed cylindrical projectile, (10) gun barrel, (11) pusher, (12) ring specimen and (13) sabot.

Kipp and Grady [12].

Table 1 includes for all successful tests performed: specimen identification, outer diameter of the ring (D_{ext}), initial thickness (t_0), initial width (w_0), impact velocity (v_z), estimated nominal circumferential strain rate ($\dot{\varepsilon}_\theta$), average fragment length (along the circumferential direction of the specimen) with standard deviation ($\overline{L}_\theta \pm SD$), average fragment thickness (along the radial direction of the specimen) with standard deviation ($\bar{t} \pm SD$), average fragment width (along the axial direction of the specimen) with standard deviation ($\overline{w} \pm SD$), average fragment mass with standard deviation ($\overline{m} \pm SD$), number of fragments based on the video recordings (N_v), number of fragments recovered (N_r) and percentage of mass recovered with respect to the complete ring ($\hat{m}$). Despite in some experiments we recover all the visible fragments, the mass of the fragments never matches the mass of the ring before testing, most likely due to material particles and debris ejected during cracks formation and fragmentation (see Figures 8 and 13). A complete summary with separate data for each specimen, including the length, thickness, width and weight of each fragment recovered is provided in Appendix A. Following the same systematic procedure employed by Nieto-Fuentes et al. [19], the length, thickness, and width of each fragment was measured in three different positions using a digital caliper with 0.01 mm of resolution. The mean value of the three measurements corresponds to L_θ, t and w, in the data sets of Appendix A. The average of all the values of L_θ, t, and w obtained per tested ring gives the average fragment length $\overline{L}_\theta$, the average fragment thickness $\bar{t}$, and the average fragment width $\overline{w}$ included in Table 1. Moreover, Appendix B includes post-mortem photographs of the recovered fragments corresponding to all specimens tested. Fragments are arranged in a layout that recreates the ring before testing.

Table 1: The dynamic fragmentation experimental campaign comprises 34 experiments: specimen label, external diameter (D_{ext}), initial thickness (t_0), initial width (w_0), impact axial velocity (v_z), estimated nominal circumferential strain rate ($\dot{\varepsilon}_\theta$), average fragment length with standard deviation ($\overline{L}_\theta \pm$ SD), average fragment thickness with standard deviation ($\bar{t} \pm$ SD), average fragment width with standard deviation ($\overline{w} \pm$ SD), average fragment mass with standard deviation ($\overline{m} \pm$ SD), number of fragments based on video recordings (N_v), number of fragments recovered (N_r) and percentage of mass recovered with respect to the complete ring ($\widehat{m}$).

Specimen	D_{ext} (mm)	t_0 (mm)	w_0 (mm)	v_z (m/s)	$\dot{\varepsilon}_\theta$ (s^{-1})	$\overline{L}_\theta \pm$ SD (mm)		$\bar{t} \pm$ SD (mm)		$\overline{w} \pm$ SD (mm)		$\overline{m} \pm$ SD (g)		N_v	N_r	$\widehat{m}$ (%)
Ring-Alu-S-1	18.08	2.00	1.76	246.4	9849.7	7.27	1.39	1.90	0.01	1.79	0.01	0.049	0.011	8	6	60.76
Ring-Alu-S-2	18.08	1.98	1.77	324.7	12961.6	6.02	1.70	1.88	0.01	1.80	0.02	0.041	0.012	9	5	42.32
Ring-Alu-S-3	18.03	1.96	1.85	385.0	15394.9	6.19	1.61	1.90	0.01	1.81	0.02	0.043	0.012	9	5	45.03
Ring-Alu-S-4	18.08	1.96	1.89	205.5	8190.1	9.96	3.70	1.90	0.02	1.78	0.01	0.070	0.026	8	5	72.67
Ring-Alu-S-5	18.07	1.97	1.75	217.9	8695.8	10.10	3.46	1.89	0.01	1.69	0.03	0.065	0.020	6	5	66.99
Ring-Alu-S-6	18.07	1.95	1.78	258.0	10286.2	8.67	2.94	1.91	0.02	1.70	0.04	0.061	0.023	8	4	51.26
Ring-Alu-S-7	18.05	1.96	1.86	327.0	13060.9	7.07	2.49	1.90	0.01	1.82	0.04	0.053	0.021	10	6	66.61
Ring-Alu-S-8	18.05	1.94	1.87	363.2	14491.9	5.61	2.04	1.88	0.03	1.81	0.04	0.041	0.015	10	9	77.05
Ring-Alu-S-9	18.08	1.97	1.8	203.3	8107.5	7.65	2.90	1.93	0.03	1.93	0.03	1.798	0.011	6	4	53.90
Ring-Alu-S-10	17.92	1.90	2.1	211.7	8490.5	9.11	3.79	1.82	0.02	1.82	0.02	2.000	0.012	6	6	98.73
Ring-Alu-S-11	17.91	1.91	2.0	258.3	10375.1	7.29	2.21	1.84	0.02	1.84	0.02	1.971	0.008	8	8	98.93
Ring-Alu-S-12	17.91	1.90	2.1	259.3	10405.8	8.28	2.13	1.80	0.02	1.80	0.02	1.999	0.010	7	7	97.48
Ring-Alu-S-13	17.94	1.91	2.1	338.7	13580.2	6.44	1.29	1.82	0.02	1.82	0.02	1.979	0.019	10	8	83.09
Ring-Alu-S-14	17.89	1.89	2.1	334.5	13436.4	7.38	2.15	1.82	0.01	1.82	0.01	2.008	0.011	9	8	95.62
Ring-Alu-S-15	17.94	1.89	2.1	367.5	14718.0	6.02	1.34	1.80	0.02	1.80	0.02	1.991	0.012	10	9	87.66
Ring-Alu-S-16	17.91	1.91	2.0	369.3	14831.5	6.11	1.79	1.80	0.02	1.80	0.02	1.976	0.008	11	9	96.59
Ring-Alu-S-17	17.92	1.87	2.1	368.8	14770.8	6.12	2.00	1.80	0.02	1.80	0.02	1.991	0.010	10	7	73.64
Ring-Alu-S-18	17.87	1.86	2.1	331.7	13316.1	5.38	2.40	1.81	0.01	1.81	0.01	2.016	0.012	10	7	59.92
Ring-Alu-S-20	17.91	1.90	2.1	207.2	8318.9	11.26	3.93	1.85	0.03	1.85	0.03	2.014	0.015	5	5	99.79
Ring-Alu-P-1	18.18	2.04	1.95	204.5	8143.0	16.21	2.59	1.97	0.01	1.87	0.03	0.133	0.018	4	3	71.00
Ring-Alu-P-2	18.18	2.07	1.97	254.0	10136.1	7.74	2.64	1.95	0.02	1.95	0.02	1.876	0.015	8	7	77.92
Ring-Alu-P-3	18.14	2.05	1.93	322.8	12897.3	7.56	1.57	1.94	0.04	1.94	0.04	1.860	0.019	7	7	87.86
Ring-Alu-P-4	18.19	2.06	1.97	371.5	14806.2	6.90	2.60	1.90	0.02	1.90	0.02	1.865	0.012	8	8	87.68
Ring-Alu-P-5	18.16	2.03	1.92	197.1	7855.7	11.60	3.40	1.95	0.03	1.95	0.03	1.842	0.032	5	5	85.55
Ring-Alu-P-6	18.10	2.00	1.94	247.2	9870.6	8.74	2.83	1.96	0.02	1.96	0.02	1.881	0.032	7	7	88.92
Ring-Alu-P-7	18.70	2.30	1.99	334.2	13094.0	8.64	2.67	1.95	0.02	1.95	0.02	1.900	0.028	7	7	93.18
Ring-Alu-P-8	18.18	2.06	2.03	371.9	14828.9	6.75	2.62	1.93	0.02	1.93	0.02	1.923	0.017	9	6	77.39
Ring-Alu-P-10	18.02	2.01	2.27	367.6	14756.9	5.54	1.44	1.91	0.02	1.91	0.02	2.204	0.026	11	10	86.17
Ring-Alu-P-11	18.00	2.01	2.23	328.3	13196.7	8.36	1.81	1.93	0.03	1.93	0.03	2.141	0.015	7	7	99.46
Ring-Alu-P-12	18.01	2.01	2.25	252.5	10140.4	10.46	3.14	1.92	0.03	1.92	0.03	2.180	0.011	6	5	90.99
Ring-Alu-P-13	17.98	1.99	2.22	253.6	10195.6	11.05	3.68	1.93	0.01	1.93	0.01	2.176	0.014	5	5	97.67
Ring-Alu-P-15	17.96	2.00	2.19	204.0	8217.5	9.76	2.76	1.89	0.03	1.89	0.03	2.158	0.012	6	6	99.46
Ring-Alu-P-16	17.95	1.99	2.22	368.2	14824.9	7.81	2.68	1.90	0.02	1.90	0.02	2.204	0.021	8	7	93.68
Ring-Alu-P-17	17.99	1.98	2.22	317.6	12746.8	8.24	2.97	1.90	0.01	1.90	0.01	2.143	0.019	7	6	85.56

3.1. Salient results

Figure 4 shows snapshots of the impact test on specimen Ring-Alu-S-4. The ring was printed with quality *standard*. The notation t $<$ 0 and t $>$ 0 is used to determine pre- and post-impact loading times, respectively, so that t = 0 µs corresponds to the impact time. The striker velocity is $v_z = 205.5$ m/s (the firing pressure was $P = 22.7$ bar). The corresponding estimated strain rate is ≈ 8190 s^{-1}. This experiment lies within the impact velocity range 1 (see Section 2), and it has been chosen to illustrate the impact process because of the quality of the image recording and the clear identification of the fracture sites. The snapshots on the left were taken by camera 1, while those on the right side correspond to camera 2, see Figure 1.

The first pair of images, snapshots (a)-(b), is taken for t = -75 µs and shows the striker approaching the pusher over which the ring specimen is inserted. Notice the alignment of the projectile trajectory with the axis of the hollow cylinder. Snapshots (c)-(d) correspond to the time of impact, t = 0 µs. The uniform contact of the projectile nose on the inner circumference of the hollow cylinder is essential for the radial expansion of the specimen, so that the strain field throughout the ring is (largely) homogeneous during loading. After the impact, the projectile penetrates the hollow cylinder, expanding it, and pushing radially outward the metal ring, see images (e)-(f). The specimen deforms as the projectile moves forward so that the first three cracks nucleate at t = 30 µs, see the colored arrows and numbering in snapshot (e). Notice that the three first cracks nucleate in the same region. This could be explained by the fact that the ring microstructure is not homogeneous (inhomogeneous spatial distribution of voids throughout the circumference of the ring, see Nieto-Fuentes et al. [19]). Three additional fractures at different locations of the ring are indicated in images (g)-(h). Note that the arrows with the same color and number in the images recorded by cameras 1 and 2 correspond to the same crack. The fragmentation has already been completed for t = 50 µs, with the formation of eight fragments of various sizes which are ejected radially outwards, moving as rigid bodies. The total time for the fragmentation process is less than 20 µs. Similar fragmentation time was obtained by Zhang and Ravi-Chandar [30] for aluminum 6061-O rings expanded at strain rates in the range $4000 - 10000$ s^{-1}. Note that the duration of the experiment and of the fragmentation process is in both cases much larger than the propagation time of (elastic) stress waves across the thickness of the specimen (≈ 0.4 µs). This indicates that each section of the ring is in equilibrium in the radial direction (this is not the case in the circumferential direction since the time of propagation of a stress wave along the specimen circumference is about 10 µs, which is consistent with the duration of the fragmentation process). The recovered fragments, arranged in a layout that recreates the ring before testing, are shown in Figure 5. They have different lengths, ranging from 14.31 mm for fragment 1, to 5.01 mm for fragment 5 (see Table A.4). Based on the video recordings, three fragments are missing, which correspond to 27.33% of the total mass of the specimen, i.e., the missing fragments are relatively small. Following Cliche and Ravi-Chandar [2], the location of the fracture sites is most likely determined by the activation of geometrical and material defects (large pores and printing defects are observed in the fractography analysis of the fracture surfaces, see Figure 6), and the size of the fragments by the distance traveled by the relieving stress waves released by early fractures. The fragmentation mechanisms for printed AlSi10Mg, which has a relatively low tensile ductility (see discussion below), seem to be consistent with the statistical fragmentation theories of Mott [18] and Grady et al. [7], rather than to the stability analysis approach of Molinari and co-workers [3, 16, 17], which is suitable for materials with large ductility in which the formation of multiple necks precedes fragmentation. Moreover, note that the cross-sectional area of the post-mortem specimen Ring-Alu-S-4 is relatively uniform, being $\approx 91\%$ in average of the initial cross section. Hence, assuming volume conservation, the average logarithmic circumferential strain in the tested specimen is $\varepsilon_\theta \approx 0.09$ (recall that this material shows relatively low tensile ductility, e.g., see Soni et al. [23]). No necks are observed and the fractures are not preceded by a local reduction of the thickness. These observations are consistent with the fragmentation patterns observed by Nieto-Fuentes et al. [19] in the axial penetration of additively-manufactured AlSi10Mg thin-walled tubes. Figure 6 shows high-magnification SEM micrographs of the fracture surface indicated in Figure 5 with a yellow arrow. The analysis is focused on the areas of the fracture surface denoted by A and B, see subplot (a). A considerable amount of pores is observed, most of them having a nearly circular section, with sizes ranging from a few micrometers up to ≈ 90 µm in diameter, see the white arrows in subplots (b), ..., (g). Recall that Nieto-Fuentes et al. [19] performed X-ray tomography measurements on additively-manufactured AlSi10Mg thin-walled tubes of 1 mm thickness printed with quality *standard*, and estimated the initial porosity to be $\approx 6\%$. Most of the pores are solidification defects formed during the manufacturing process – mainly lack of fusion and gas porosity – and they do not seem to have nucleated/growth during the deformation of the specimen, especially the larger ones (yet, some of them show internal cracks, see the green arrows in subplots (e)-(f)). The fracture surface is a succession of circular cross-sectional cavities connected by ductile fracture areas, e.g., see red arrows in subplots (b), ..., (g). The fracture surfaces looked alike for other fragments, however, the corresponding SEM micrographs are not shown for the sake of brevity.

Figure 7 shows a sequence of images of the test on specimen Ring-Alu-P-5. The ring was printed with quality *performance*. This test is selected for the analysis because the impact velocity is $v_z = 197.1$ m/s, i.e., only 4% lower than for Ring-Alu-S-4 – the test on specimen Ring-Alu-P-5 also lies within the impact velocity range 1.

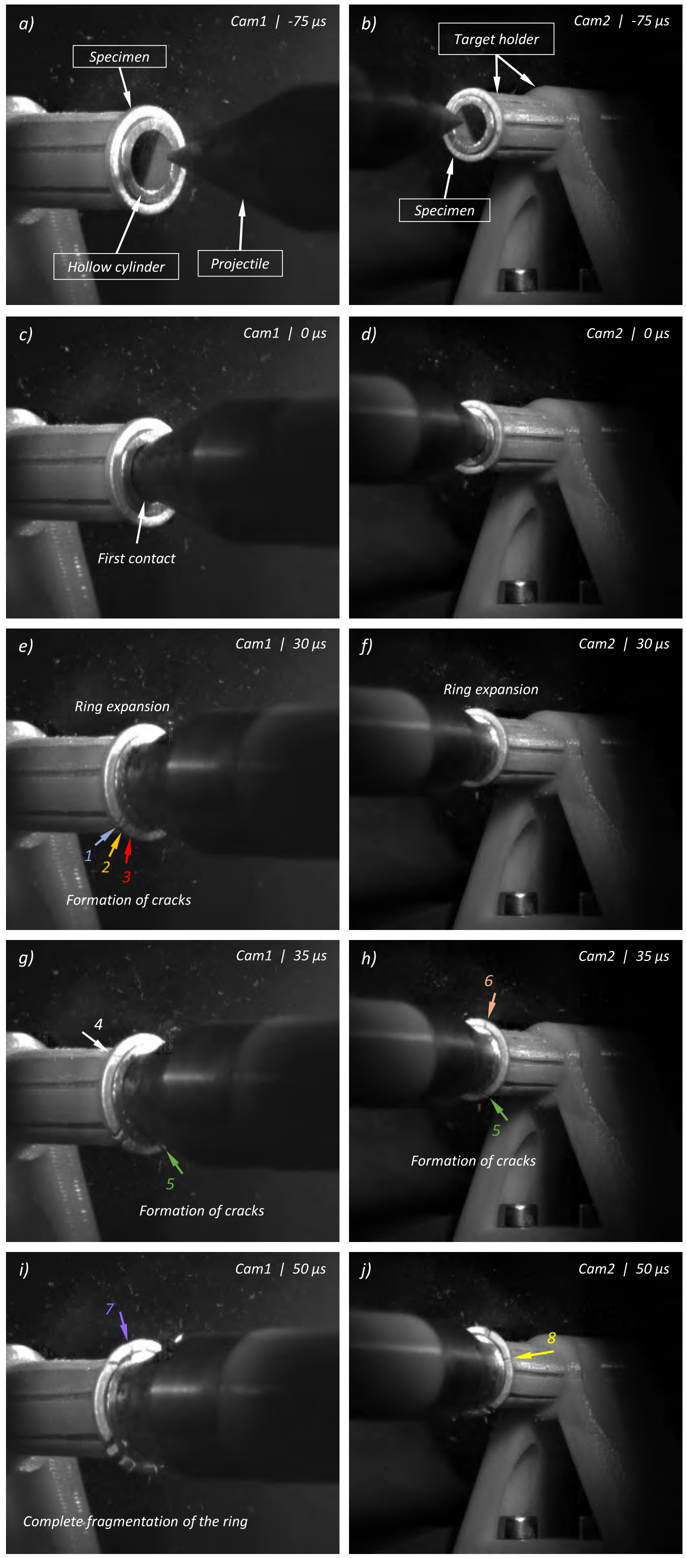

Figure 4: Sequence of images of the impact test for specimen Ring-Alu-S-4 for different loading times: (a)-(b) t = −50 µs, (c)-(d) t = 0 µs, (e)-(f) t = 30 µs, (g)-(h) t = 35 µs and (i)-(j) t = 50 µs. Images obtained by camera 1 are on the left side of the sequence, while those obtained by camera 2 are on the right side. The impact velocity is v_z = 205.5 m/s. The arrows with the same color and number in the images recorded by cameras 1 and 2 correspond to the same crack. For interpretation of the references to color in this figure, the reader is referred to the web version of this article.

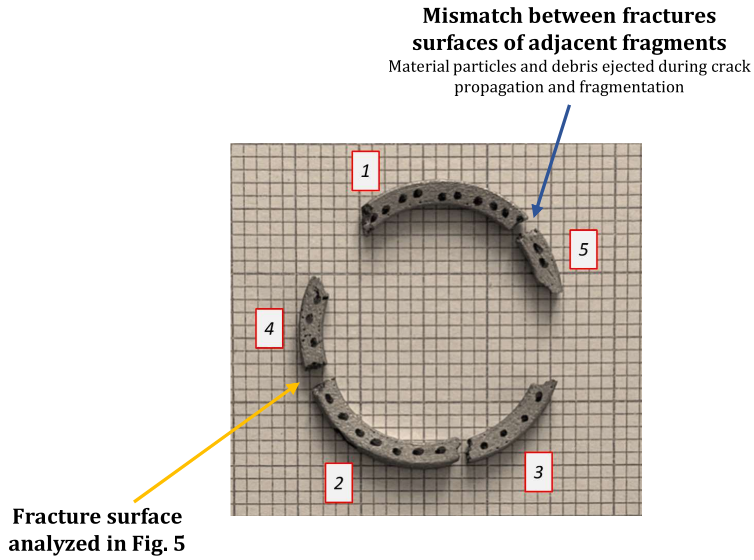

Figure 5: Post-mortem photography of the recovered fragments corresponding to specimen Ring-Alu-S-4. Fragments arranged in a layout that recreates the ring before testing. As to the number of fragments observed in the video recordings, three fragments are missing, which correspond to 27.33% of the total mass of the specimen. The width, length, thickness and weight of the recovered fragments is given in Table A.4. The impact velocity is $v_z = 205.5$ m/s.

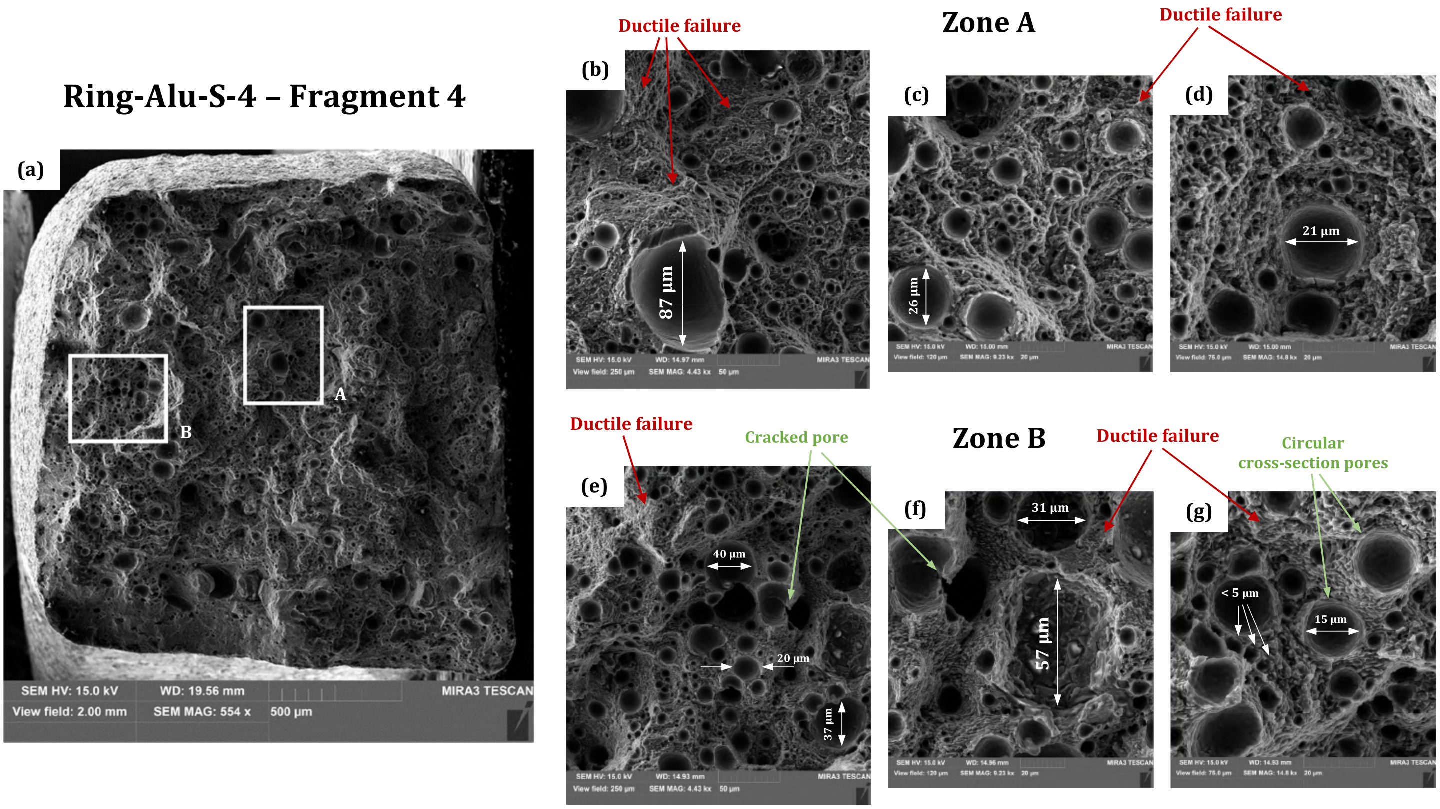

Figure 6: High-magnification SEM micrographs of fracture surface corresponding to fragment 4 of specimen Ring-Alu-S-4 indicated in Figure 5 with yellow arrow. The impact velocity is $v_z = 205.5$ m/s. For interpretation of the references to color in this figure, the reader is referred to the web version of this article.

The shooting pressure was $P = 24$ bar. Snapshots from (a) to (d) show the striker approaching the target and impacting (rather) uniformly along the inner perimeter of the hollow cylinder. For 25 µs, the ring has already fractured at three places which are indicated with colored arrows in images (e)-(f). Recall that the arrows with the same color and number in the images recorded by cameras 1 and 2 correspond to the same crack. For 40 µs the specimen is completely fragmented, the arrows in snapshots (g)-(h) indicating the two additional fractures that occurred within the interval 25 µs < t < 40 µs, so that the ring breaks up into 5 fragments which are shown in Figure 8. The fragments have different lengths ranging from 15.32 mm for fragment 1 to 5.91 mm for fragment 2 (see Table A.24). The fractures occurred without previous necking, similarly to the test on Ring-Alu-S-4. The average cross-sectional area of the post-mortem sample is ≈ 96% of the initial cross section, so that the average logarithmic circumferential strain in the tested specimen is $\varepsilon_\theta \approx 0.04$ (further analysis on the permanent strain in the tested rings for different impact velocities is performed in Section 3.2). Figure 9 shows high-magnification SEM micrographs of the fracture surface indicated in Figure 8 with a yellow arrow. The analysis is focused on the area denoted by A, see subplot (a). The micrographs of the crack surface show many pores with nearly circular cross section, yet, less than in the case of the specimen Ring-Alu-S-4 printed with quality *standard*, for which larger voids were observed (compare Figures 6 and 9). Note that the cross section of the pores in the micrographs of the Ring-Alu-P-5 sample is generally less than 20 µm in diameter, and many of them are smaller than 5 µm. The X-ray tomography measurements performed by Nieto-Fuentes et al. [19] on AlSi10Mg thin-walled tubes of 1 mm thickness printed with quality *performance* showed the initial void volume fraction to be ≈ 2% (approximately 3 times less than in the sample printed with quality *standard*). Nevertheless, note that, despite of the differences in initial void volume fraction and distribution of pore sizes between *standard* and *performance* specimens, the video recordings of the tests did not bring out any significant difference in the fragmentation mechanisms of samples Ring-Alu-P-5 and Ring-Alu-S-4. This conclusion will be further substantiated with the results presented in Section 3.2.

3.2. The effect of impact velocity

Figure 10 shows snapshots of the test on specimen Ring-Alu-S-3 within the time interval -45 µs $\leq$ t $\leq$ 35 µs. The impact velocity is $v_z = 385$ m/s (the shooting pressure was $P = 95$ bar), i.e., almost twice larger than in the test on the *standard* specimen Ring-Alu-S-4 shown in Figure 4. The experiment on specimen Ring-Alu-S-3 lies within the impact velocity range 4 (see Section 2). The striker travels centered with respect to the axis of the target, see images (a)-(b), such that the impact is uniform all along the inner perimeter of the hollow cylinder, see images (c)-(d). The time interval from the first contact to the uniform expansion of the hollow cylinder seems to

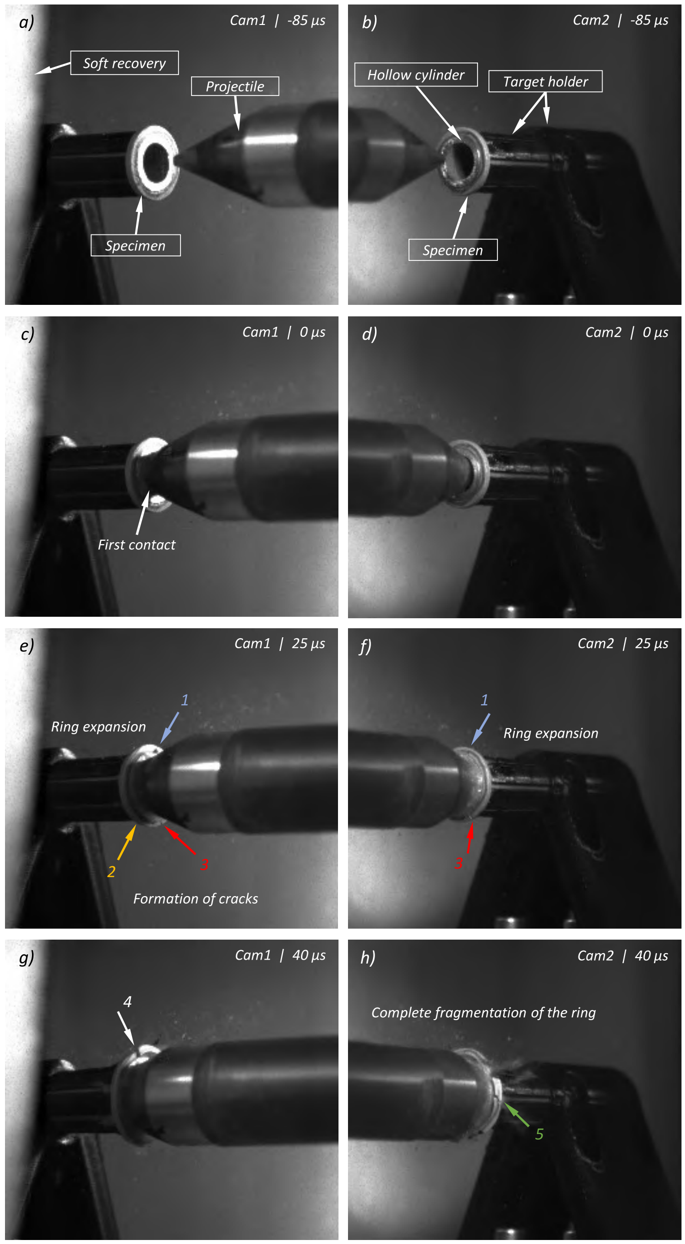

Figure 7: Sequence of images of the impact test for specimen Ring-Alu-P-5 for different loading times: (a)-(b) t = −85 µs, (c)-(d) t = 0 µs, (e)-(f) t = 25 µs and (g)-(h) t = 40 µs. Images obtained by camera 1 are on the left side of the sequence, while those obtained by camera 2 are on the right side. The impact velocity is v_z = 197.1 m/s. The arrows with the same color and number in the images recorded by cameras 1 and 2 correspond to the same crack. For interpretation of the references to color in this figure, the reader is referred to the web version of this article.

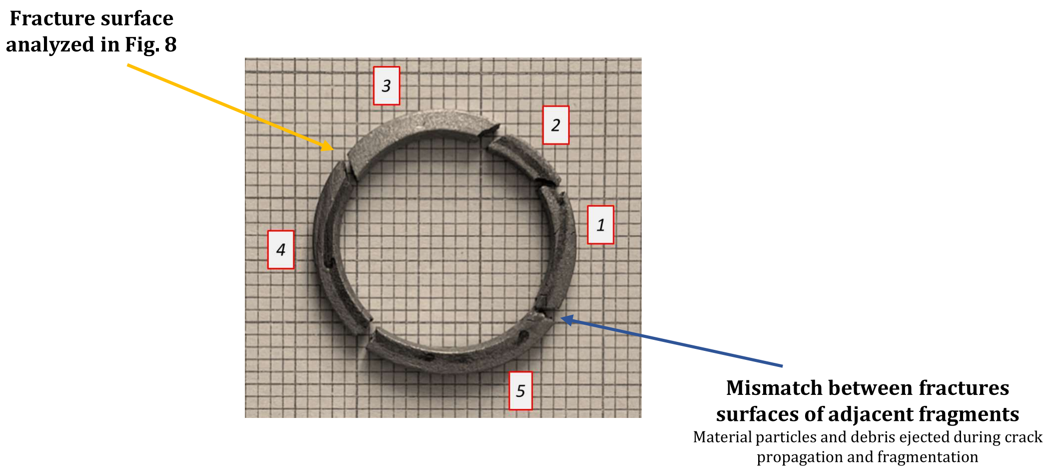

Figure 8: Post-mortem photography of the recovered fragments corresponding to specimen Ring-Alu-P-5. Fragments arranged in a layout that recreates the ring before testing. The width, length, thickness and weight of the recovered fragments is given in Table A.4. The impact velocity is $v_z = 191.1$ m/s.

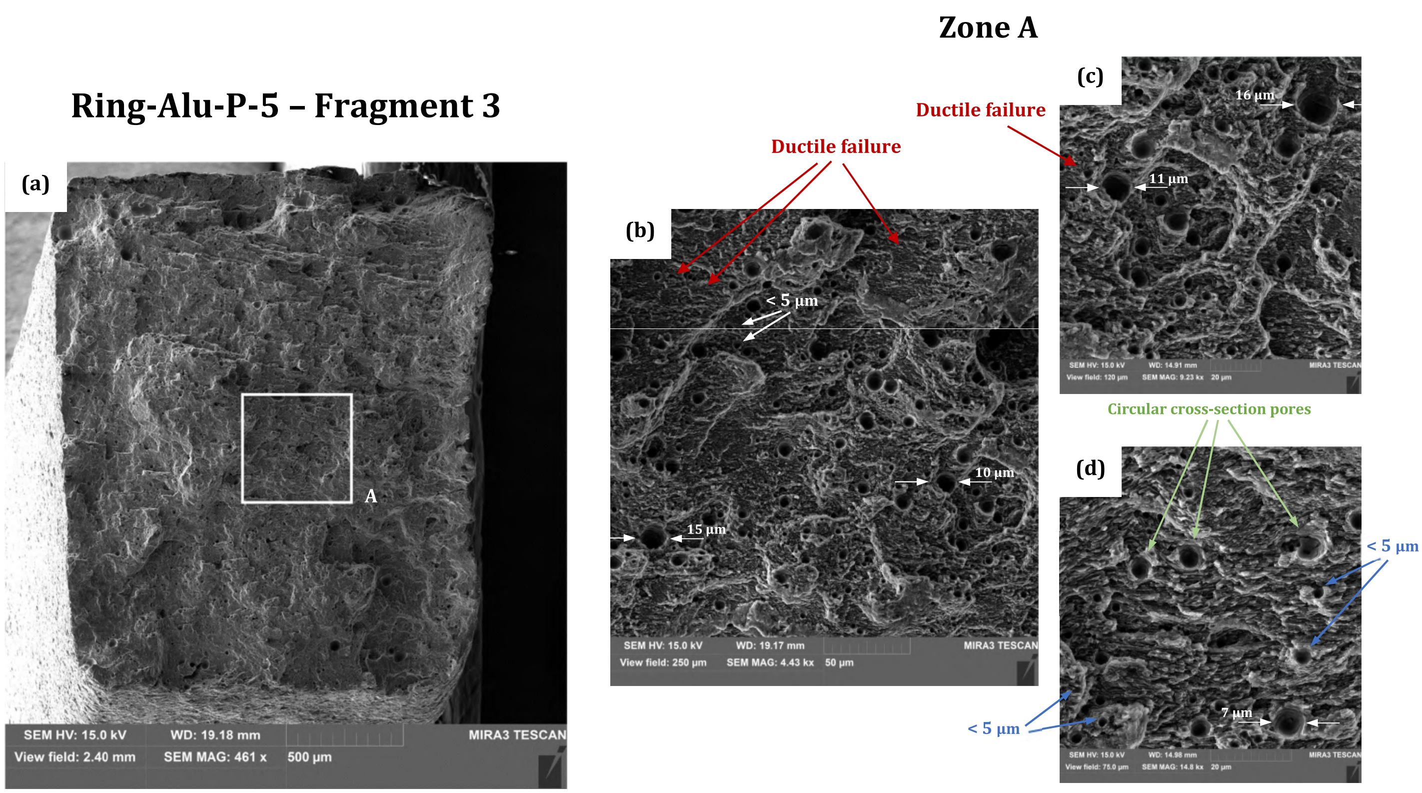

Figure 9: High-magnification SEM micrographs of fracture surface corresponding to fragment 3 of specimen Ring-Alu-P-5 indicated in Figure 8 with yellow arrow. The impact velocity is $v_z = 191.1$ m/s. For interpretation of the references to color in this figure, the reader is referred to the web version of this article.

be less than 5 µs (less than 2 mm of projectile axial displacement). For a loading time of 10 µs, there are 4 cracks throughout circumference of the specimen, and 5 more nucleate before the loading time reaches 15 µs, leading to a total of 9 fragments of different sizes, out of which 5 are recovered and shown in Figure 11. Note that the number of fragments increased from 8 to 9 with respect to sample Ring-Alu-S-4 which was tested at half speed (we refer to the actual number of fragments as seen in the video recordings, see Table 1). A complete analysis on the increasing number of fragments with the impact velocity will be shown later in this section of the paper. The average cross section of the recovered fragments is 95% of the initial size of the sample, so that the permanent logarithmic circumferential strain in the specimen is ≈ 0.05.

Images of the video recording of the impact on specimen Ring-Alu-P-4 are included in Figure 12. Compared to the test on Ring-Alu-P-5 shown in Figure 7, the impact velocity is 88% greater (namely, 371.5 m/s for a shooting pressure of 89.1 bar). The test on specimen Ring-Alu-P-4 lies within the impact velocity range 4. Eight fractures are nucleated in the ring within a time interval of less than 30 µs. The fragmentation process starts at 15 µs with the cracks indicated in snapshots (e)-(f), and it is completed with the fractures identified in snapshots (i)-(j), which show free radial flying of the fragments. The post-mortem measurement of the recovered fragments, see Figure 13, shows that the average cross section of the ring after testing is $\approx$ 88% of the initial size, so that the average permanent circumferential logarithmic strain is 0.12. Notice that the strain in the sample after testing does not follow any specific trend with the impact velocity and the printing quality (compare the values of permanent logarithmic circumferential strain obtained for Ring-Alu-S-3, Ring-Alu-S-4, Ring-Alu-P-4 and Ring-Alu-P-5). The scatter in the strain at fragmentation is attributed to the porosity and the surface roughness of the specimens, which act as material and geometrical defects, leading to large variability in the ductility of the rings (Weavwe and Rosenthal [27] argued the scatter in ductility of additively-manufactured metals to be caused by significant variation in defects). Note also that the scatter in the tensile ductility of additively-manufactured AlSi10Mg samples has been previously reported by Kristoffersen et al. [13]. On the other hand, as compared with the specimen Ring-Alu-P-5 tested at lower speed, the number of fragments has increased from 5 to 8, consistent with the general trend that more fractures are nucleated at higher impact velocity.

The evolution of the number of fragments identified in the video recordings with the impact velocity is shown in Figure 14. The four velocity ranges investigated are identified and enclosed with dashed grey lines. Results of all tests performed are included, the black markers corresponding to the rings printed with quality *standard* and

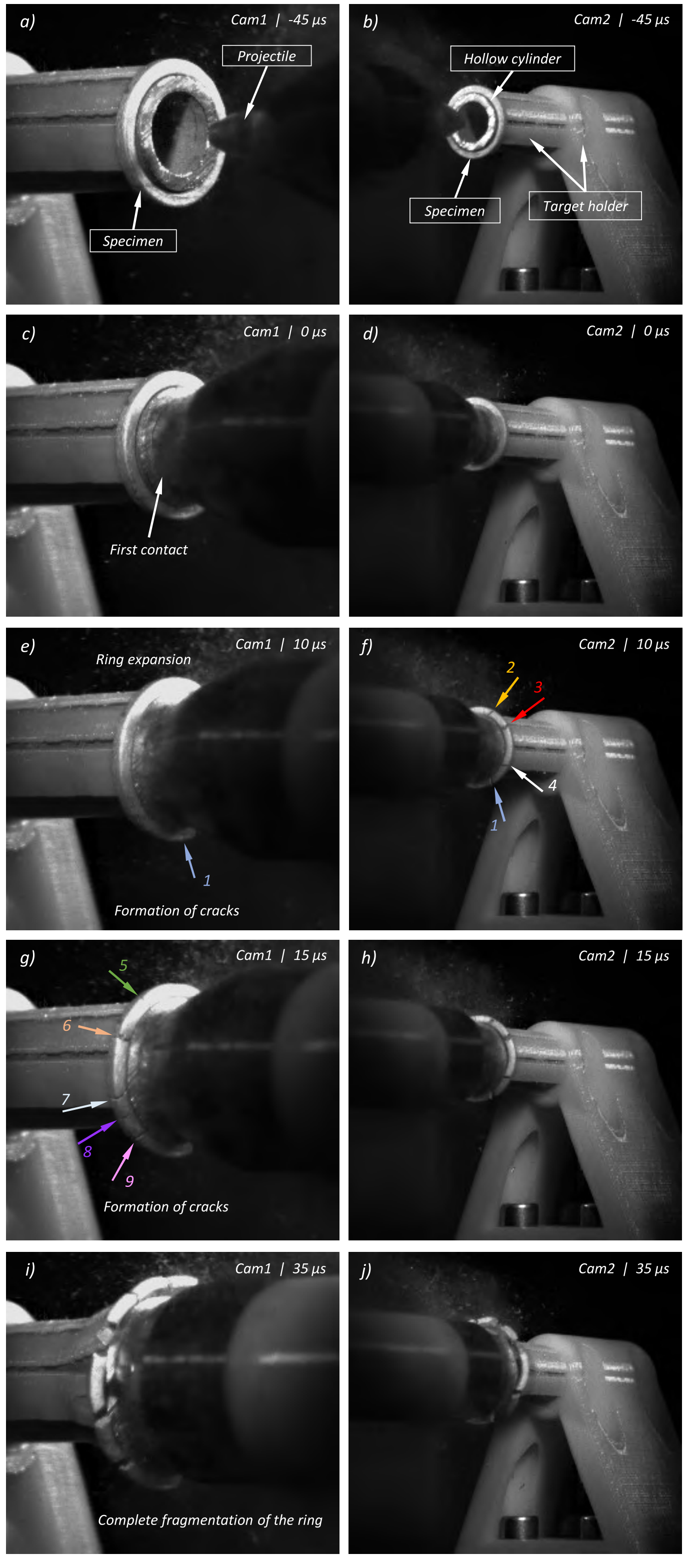

Figure 10: Sequence of images of the impact test for specimen Ring-Alu-S-3 for different loading times: (a)-(b) t = −45 μs, (c)-(d) t = 0 μs, (e)-(f) t = 10 μs, (g)-(h) t = 15 μs and (i)-(j) t = 35 μs. Images obtained by camera 1 are on the left side of the sequence, while those obtained by camera 2 are on the right side. The impact velocity is v_z = 385 m/s. The arrows with the same color and number in the images recorded by cameras 1 and 2 correspond to the same crack. For interpretation of the references to color in this figure, the reader is referred to the web version of this article.

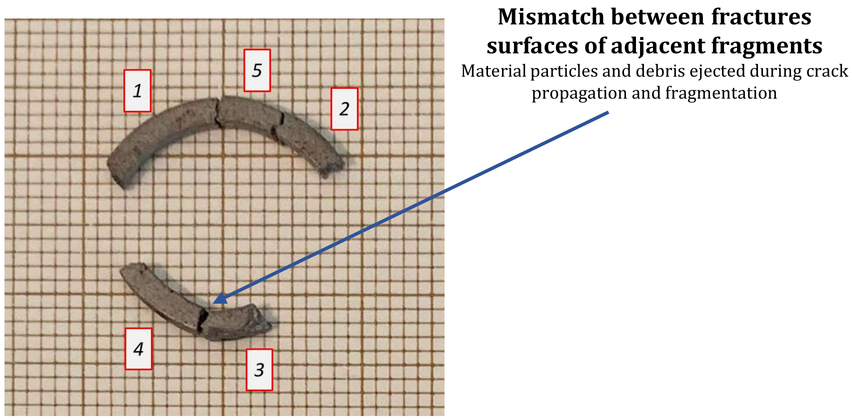

Figure 11: Post-mortem photography of the recovered fragments corresponding to specimen Ring-Alu-S-3. Fragments arranged in a layout that recreates the ring before testing. As to the number of fragments observed in the video recordings, four fragments are missing, which correspond to 54.97% of the total mass of the specimen. The width, length, thickness and weight of the recovered fragments is given in Table A.3. The impact velocity is $v_z = 385$ m/s.

the red markers to the *performance* specimens. The *standard* specimens seem to break up into more fragments (this observation is consistent with Wood et al. [29], who performed experiments with 718 Inconel printed rings and concluded that the number of fragments increases with increasing porosity, see Section 1). However, more experiments are needed to draw definite conclusions on the influence of the printing quality in the number of fragments, so that the experiments obtained with both *standard* and *performance* specimens have been fitted to a single power-type function (the values of the coefficients are given in the plot legend). According to the fitted curve, raising the impact velocity from 200 m/s to 400 m/s shifts the number of fragments from 6 to 10 (these are rounded numbers, as providing the number of fragments with decimal digits lacks of physical meaning). The same qualitative results and general trend have been obtained by Grady and Olsen [8] and Altynova et al. [1] for experiments carried out with U6N and 6061 aluminum rings. Moreover, a comparison is performed with the theory of Kipp and Grady [12], which computes the number of fragments using the following equation:

$$N_{Kipp-Grady} = 2\pi R_m \left(\frac{\rho_0 \; \dot{\varepsilon}_\theta^2}{24 \; \gamma} \right)^{\frac{1}{3}} \tag{1}$$

where R_m is the mean radius of the ring (see Table 1), ρ_0 is the initial material density, $\dot{\varepsilon}_\theta$ is the circumferential strain rate in the specimen (see Table 1), and γ is the fracture energy (which in porous materials has been shown to decrease with the initial void volume fraction, see e.g. Pardoen and Hutchinson [21]). The fracture energy – following the work of Thomason [25] – was computed as $\gamma = 0.4k\delta$, where $k = \sigma_u/\sqrt{3}$ is the ultimate shear stress (σ_u being the ultimate tensile strength) and δ is the average distance between pores, which was estimated using the mean void equivalent diameters and void volume fractions reported by Nieto-Fuentes et al. [19] for *standard*

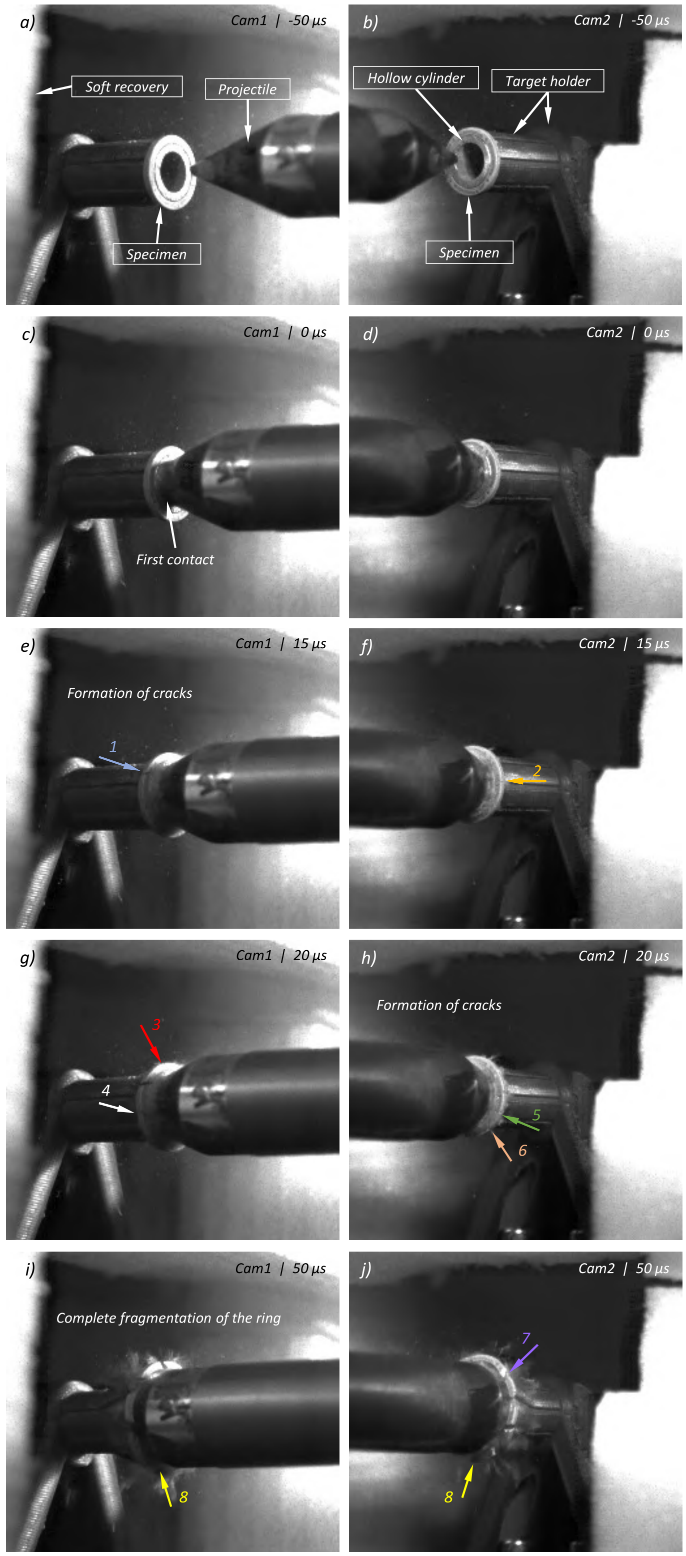

Figure 12: Sequence of images of the impact test for specimen Ring-Alu-P-4 for different loading times: (a)-(b) t = −50 µs, (c)-(d) t = 0 µs, (e)-(f) t = 15 µs, (g)-(h) t = 20 µs and (i)-(j) t = 50 µs. Images obtained by camera 1 are on the left side of the sequence, while those obtained by camera 2 are on the right side. The impact velocity is v_z = 371.5 m/s. The arrows with the same color and number in the images recorded by cameras 1 and 2 correspond to the same crack. For interpretation of the references to color in this figure, the reader is referred to the web version of this article.

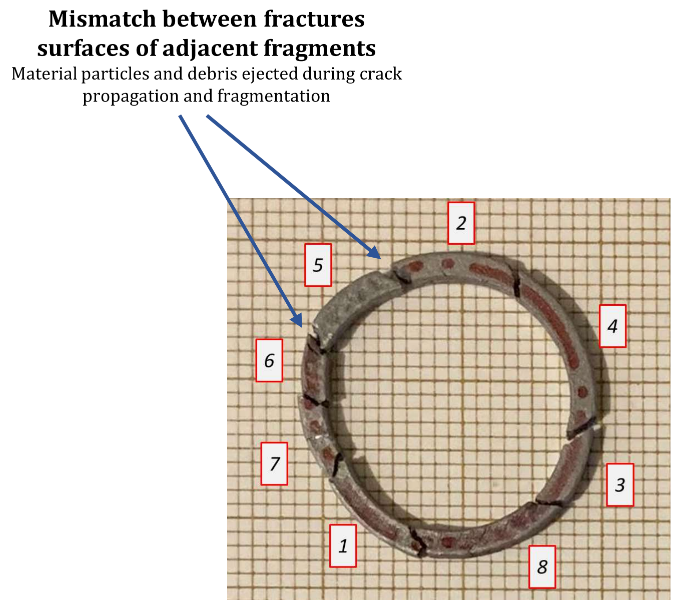

Figure 13: Post-mortem photography of the recovered fragments corresponding to specimen Ring-Alu-P-4. Fragments arranged in a layout that recreates the ring before testing. The width, length, thickness and weight of the fragments is given in Table A.23. The impact velocity is $v_z = 371.5$ m/s.

and *performance* AlSi10Mg samples. The values of the material parameters used in Equation (1) to compute the results of Figure 14 are shown in Table 2. Note in Figure 14 that the theory of Kipp and Grady [12] predicts results which are in quantitative agreement with the experiments, and it is able to capture the trend of increasing number of fragments as the impact velocity increases, for the whole range of impact velocities investigated. Notice also that the theory predicts that for the same impact velocity the number of fragments is larger for the *standard* samples, as the fracture energy depends on the average distance between pores – this being smaller in the case of *standard* specimens.

Table 2: Values of the parameters used to compute the number of fragments with the theory of Kipp and Grady [12], see Equation (1). The values of the initial density and the ultimate tensile strength are taken from the data sheet provided by Materialise NV [15].

Symbol	Property and units	*Standard*	*Performance*
ρ_0	Initial density (kg/m^3)	2590	2650
σ_u	Ultimate tensile strength (MPa)	250	300
γ	Fracture energy (J/m^2)	3795.4	5081.3

The recovered fragments length distributions for all the tests performed are shown in Figure 15, collected into four histograms which account for the four impact velocity ranges investigated, see Section 2: (a) 197 m/s $\leq v_z \leq$ 218 m/s, (b) 246 m/s $\leq v_z \leq$ 259 m/s, (c) 317 m/s $\leq v_z \leq$ 338 m/s and (d) 363 m/s $\leq v_z \leq$ 385 m/s. The black and red blocks correspond to the results obtained from *standard* and *performance* specimens, respectively. The

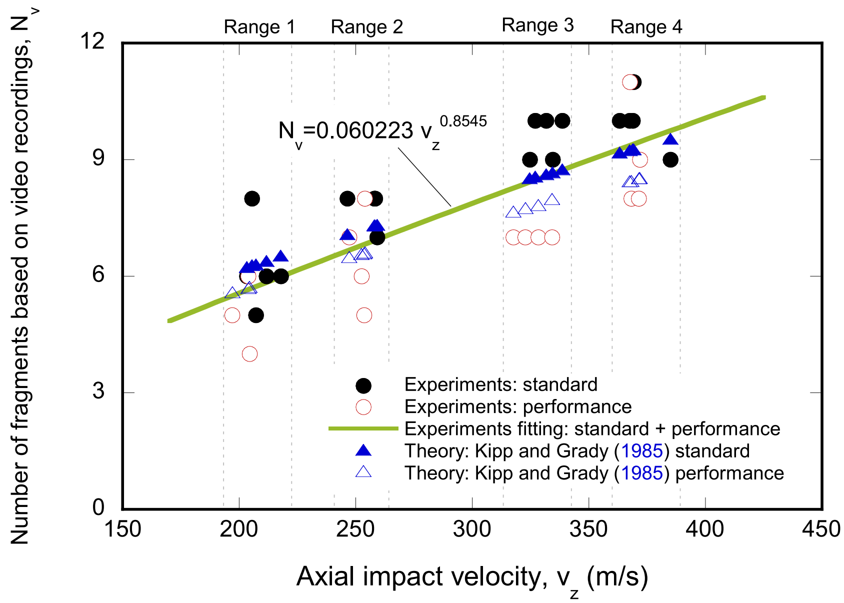

Figure 14: Evolution of the number of fragments identified in the video recordings N_v with the impact velocity v_z. Comparison with the predictions obtained from the fragmentation theory of Kipp and Grady [12].

height of a colored block within a bar of the histogram provides the number of fragments for a given interval of fragments length. While the *performance* samples show few larger fragments for the four impact velocity ranges, the distribution of fragment sizes for both printing qualities is very similar, qualitatively and quantitatively, so that a single Weilbull distribution function, Equation (2), was fitted to the experimental measurements including both *standard* and *performance* samples:

$$f = \frac{\kappa}{\lambda}\left(\frac{L_\theta}{\lambda}\right)^{(\kappa-1)} e^{(L_\theta/\lambda)^\kappa} \tag{2}$$

where κ and λ are the scale and shape parameters of the distribution, respectively – the values of κ and λ are given in the histograms of Figure 15. Moreover, the mean and the standard deviation of the distribution function can be computed as $\mu = \lambda\Gamma\left(1+\frac{1}{\kappa}\right)$ and $SD^2 = \lambda^2\Gamma\left(1+\frac{2}{\kappa}\right) - \mu^2$, respectively, with Γ being the gamma function. In addition, the values of the experimental mean (μ_{exp}) and standard deviation (SD_{exp}) for the four impact velocity ranges considered are given in Table 3. Notice that both the experimental average fragment length and the standard deviation decrease as the impact velocity increases, showing that the loading rate favors the formation of more fragments of similar size. In addition, the same table includes values of the relative standard deviation $RSD_{exp} = \mu_{exp}/SD_{exp}$, indicating a slight decrease in fragment length dispersion (relative to the mean) with increasing velocity – note that the relative standard deviations are considerably similar for the four velocity ranges.

These results show close resemblance with the experiments of Zhang and Ravi-Chandar [30, 31] on aluminum and copper rings, and with the numerical calculations of Cliche and Ravi-Chandar [2], which showed that the fragments distribution shifts towards smaller fragments and towards narrower distributions with increasing loading rate. The idea is that as the strain rate increases, the propagation of the release wave emanating from early fractures is limited to shorter times, so that the unloading does not travel far enough to inhibit further fractures at neighboring locations.

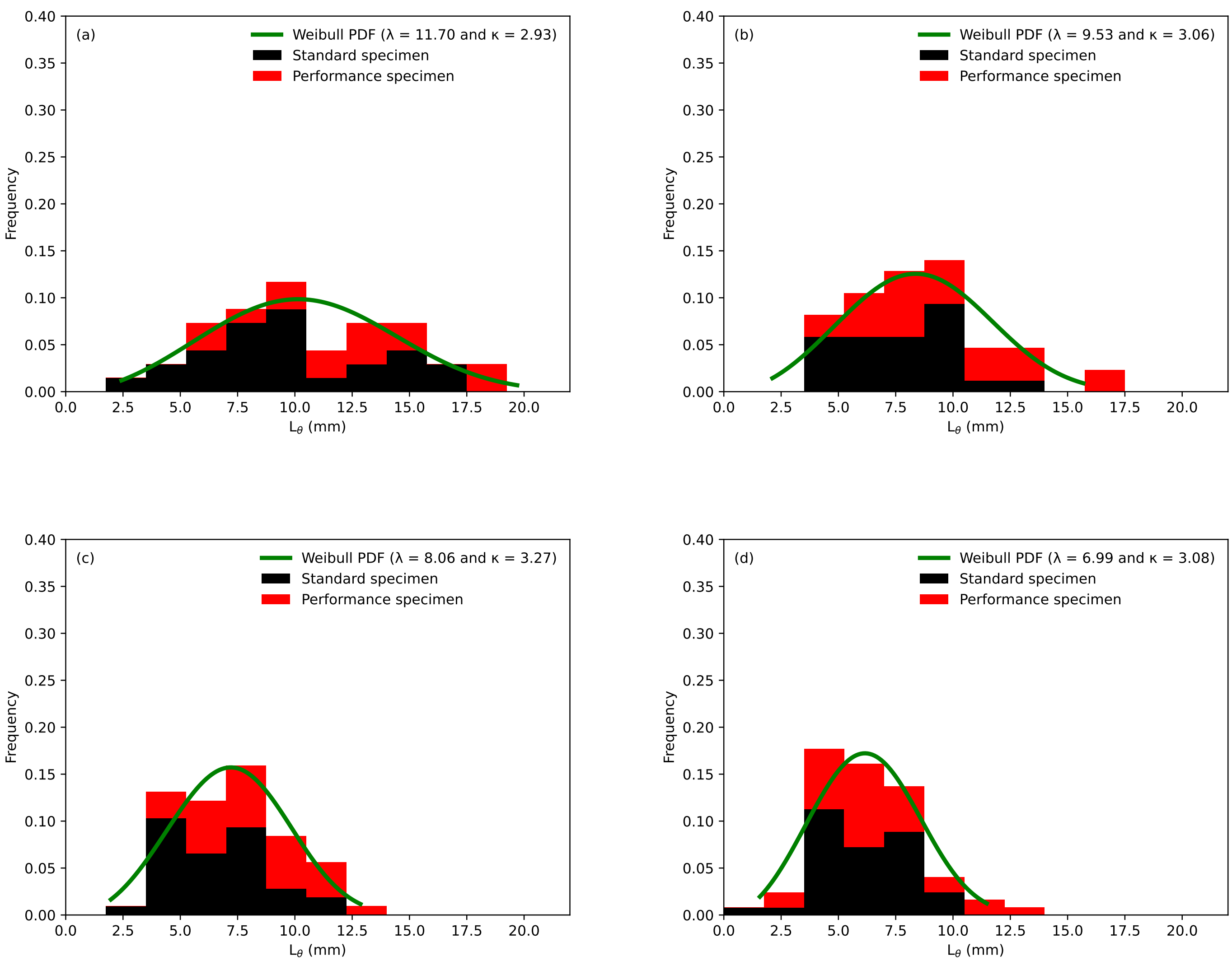

Figure 15: Distributions of fragments length L_θ which include all the fragments recovered from the impact experiments, see Tables A.1-A.34. The results are collected as a function of the impact velocity range: (a) 197 m/s $\leq v_z \leq$ 218 m/s, (b) 246 m/s $\leq v_z \leq$ 259 m/s, (c) 317 m/s $\leq v_z \leq$ 338 m/s and (d) 363 m/s $\leq v_z \leq$ 385 m/s. A Weibull probability density function, see Equation (2), was fitted to the experimental measurements (green solid line).

Table 3: Mean (μ_{exp}), standard deviation (SD_{exp}), and normalized standard deviation (RSD_{exp}) of the experimental measurements of the fragments length for the four impact velocity ranges considered, see Figure 15.

Experiments	μ_{exp} (mm)	SD_{exp} (mm)	RSD_{exp}(%)
Impact velocity range 1 (197 m/s $\leq v_z \leq$ 218 m/s)	10.41	3.96	38
Impact velocity range 2 (246 m/s $\leq v_z \leq$ 259 m/s)	8.52	2.95	35
Impact velocity range 3 (317 m/s $\leq v_z \leq$ 338 m/s)	7.22	2.41	33
Impact velocity range 4 (363 m/s $\leq v_z \leq$ 385 m/s)	6.26	2.15	34

4. Concluding remarks

In this paper, we have presented a novel experiment to investigate dynamic fragmentation of metal rings subjected to rapid radial expansion. The setup consists of a helium-driven gas gun firing a cylindrical conical-nose projectile that impacts axially a ductile hollow cylinder over which the specimen is inserted. The diameter of the cylindrical base of the striker is greater than the inner diameter of the hollow cylinder, which expands as the projectile moves forward, imparting radial momentum to the metal ring, which deforms and ultimately breaks up into multiple fragments. The ring specimens are produced by Selective Laser Melting out of AlSi10Mg using two printing qualities, *standard* and *performance*, which show different level of residual porosity and distribution of void sizes. A total of 34 successful experiments have been carried out for impact velocities ranging from 197 m/s to 385 m/s, using samples with inner diameter of 14 mm and square cross section of 4 mm^2. The tests have been recorded using two high-speed cameras which provide high-resolution images of the fragmentation process, and the fragments have been recovered, sized and weighted to obtain the statistics of the fragments size distributions. The main results drawn from this investigation are:

- The fragmentation mechanisms of *standard* and *performance* specimens are similar, such that the homogeneous expansion of the sample precedes the formation of multiple fractures throughout the circumference of the ring without previous necking.

- The location of the fracture sites seems to be determined by the activation of large pores and printing defects observed in the fractography analysis of the fracture surfaces, and the size of the fragments by the distance traveled by the relieving stress waves released by early fractures.

- The increase of impact velocity shifts the fragments size distribution towards smaller fragments, and towards narrower distributions, because the propagation of the release wave emanating from early fractures is limited to shorter times, so that the unloading does not travel far enough to inhibit further fractures at neighboring locations.

- The differences in the number of fragments, and in the fragments' size distribution, between the specimens printed with *standard* and *performance* quality are small, yet, the results suggest that there is a trend for the *performance* specimens to break into less fragments. This seems related to the fact that *standard* specimens have a larger initial porosity.

- The theory of Kipp and Grady [12], coupled with the fracture energy model proposed by Thomason [25], predicts the increasing number of fragments with the impact velocity, these results being in quantitative agreement with experiments for the whole range of impact velocities investigated. The theory is also able to predict the (slightly) larger number of fragments for *standard* specimens, due to the greater initial porosity (thus a shorter average distance between voids and, as a consequence, a lower fracture energy) compared to the *performance* ones.

These results and general trends are consistent with data obtained by different authors for the fragmentation of rings made of different metals and alloys [6, 8, 30, 31, 2, 29]. On the other hand, compared to other available techniques in which the expansion of the specimen is driven by explosives or electromagnetic loading, this experimental setup stands out for its simplicity, fast operation, and quick assembly, which facilitates to perform extensive experimental campaigns. Recall that the electromagnetic setup is suitable to test good electrical conductors with moderate flow strength, as testing high resistive and high strength materials requires more current, which leads to increased Joule heating effects (such limitations are not present in the gas gun driven setup, which shows increased flexibility to test different materials). In future works, it would be interesting to compare the results obtained with the experimental setup presented in this paper with ring expansion tests carried out with the electromagnetic expanding ring method.

Acknowledgements

The assistance of Mr. Sergio Puerta and Mr. David Pedroche in the development of the experimental setup is greatly acknowledged.

The fracture surface images reported on were taken using a MIRA3 scanning electron microscope from Tescan located at the Technion – Israel Institute of Technology – in the Computational and Experimental Micromechanics of Materials Lab lead by Dr. Shmuel Osovski.

Funding

The research leading to these results has received funding from the European Research Council (ERC) under the European Union's Horizon 2020 research and innovation programme (Project PURPOSE), grant agreement No. 758056.

J. C. Nieto-Fuentes acknowledges support from the CONEX-Plus programme funded by Universidad Carlos III de Madrid and the European Union's Horizon 2020 research and innovation programme, under the Marie Sklodowska-Curie grant agreement No. 801538.

Conflict of interest

The authors declare that they have no known competing financial interests or personal relationships that could have appeared to influence the work reported in this paper.

Author contributions

J. C. Nieto-Fuentes: Conceptualization; Data curation; Formal analysis; Investigation; Methodology; Software; Validation; Writing - original draft; Writing - review & editing. **T. Virazels**: Conceptualization; Data curation; Formal analysis; Investigation; Methodology; Software; Validation; Writing - original draft; Writing - review & editing. **N. Jacques**: Conceptualization, Methodology, Writing - review and editing. **J. A. Rodríguez-Martínez**: Conceptualization; Formal analysis; Funding acquisition; Investigation; Methodology; Project administration; Resources; Supervision; Validation; Writing - original draft; Writing - review & editing.

Appendix A. List of fragments

This section provides the width, length, thickness and weight of all fragments recovered from the impact experiments.

Table A.1: Recovered fragments for specimen Ring-Alu-S-1: length (L_θ), thickness (t), width (w) and mass (m).

Fragment	L_θ (mm)	t (mm)	w (mm)	m (g)
1	7.00	1.88	1.77	0.047
2	7.10	1.90	1.82	0.045
3	10.23	1.90	1.80	0.070
4	6.85	1.89	1.79	0.051
5	6.59	1.92	1.79	0.044
6	5.84	1.90	1.80	0.035

Table A.2: Recovered fragments for specimen Ring-Alu-S-2: length (L_θ), thickness (t), width (w) and mass (m).

Fragment	L_θ (mm)	t (mm)	w (mm)	m (g)
1	4.86	1.88	1.82	0.028
2	7.45	1.87	1.81	0.050
3	8.61	1.90	1.78	0.060
4	4.31	1.90	1.80	0.034
5	4.85	1.87	1.78	0.031

Table A.3: Recovered fragments for specimen Ring-Alu-S-3: length (L_θ), thickness (t), width (w) and mass (m).

Fragment	L_θ (mm)	t (mm)	w (mm)	m (g)
1	8.89	1.91	1.79	0.064
2	5.45	1.90	1.85	0.037
3	4.58	1.89	1.80	0.031
4	7.12	1.92	1.80	0.048
5	4.89	1.89	1.81	0.036

Table A.4: Recovered fragments for specimen Ring-Alu-S-4: length (L_θ), thickness (t), width (w) and mass (m).

Fragment	L_θ (mm)	t (mm)	w (mm)	m (g)
1	14.31	1.91	1.77	0.102
2	14.08	1.91	1.76	0.097
3	9.14	1.89	1.77	0.065
4	7.25	1.87	1.80	0.050
5	5.01	1.91	1.78	0.034

Table A.5: Recovered fragments for specimen Ring-Alu-S-5: length (L_θ), thickness (t), width (w) and mass (m).

Fragment	L_θ (mm)	t (mm)	w (mm)	m (g)
1	15.86	1.90	1.72	0.099
2	9.13	1.90	1.65	0.061
3	8.81	1.89	1.70	0.057
4	6.61	1.87	1.67	0.044
5	8.93	1.88	1.66	0.060

Table A.6: Recovered fragments for specimen Ring-Alu-S-6: length (L_θ), thickness (t), width (w) and mass (m).

Fragment	L_θ (mm)	t (mm)	w (mm)	m (g)
1	12.62	1.91	1.75	0.092
2	10.09	1.93	1.69	0.071
3	7.09	1.90	1.72	0.052
4	4.86	1.88	1.64	0.031

Table A.7: Recovered fragments for specimen Ring-Alu-S-7: length (L_θ), thickness (t), width (w) and mass (m).

Fragment	L_θ (mm)	t (mm)	w (mm)	m (g)
1	11.95	1.88	1.88	0.095
2	4.53	1.90	1.84	0.030
3	4.80	1.90	1.77	0.037
4	7.68	1.90	1.76	0.044
5	5.99	1.92	1.84	0.050
6	7.48	1.91	1.83	0.064

Table A.8: Recovered fragments for specimen Ring-Alu-S-8: length (L_θ), thickness (t), width (w) and mass (m).

Fragment	L_θ (mm)	t (mm)	w (mm)	m (g)
1	5.75	1.88	1.77	0.046
2	4.58	1.87	1.79	0.035
3	5.42	1.90	1.80	0.043
4	8.54	1.89	1.83	0.056
5	9.29	1.90	1.80	0.070
6	6.32	1.91	1.79	0.047
7	4.08	1.90	1.81	0.028
8	2.91	1.81	1.91	0.019
9	3.63	1.89	1.79	0.025

Table A.9: Recovered fragments for specimen Ring-Alu-S-9: length (L_θ), thickness (t), width (w) and mass (m).

Fragment	L_θ (mm)	t (mm)	w (mm)	m (g)
1	7.72	1.92	1.80	0.051
2	11.55	1.98	1.80	0.095
3	7.94	1.92	1.81	0.059
4	3.38	1.91	1.78	0.023

Table A.10: Recovered fragments for specimen Ring-Alu-S-10: length (L_θ), thickness (t), width (w) and mass (m).

Fragment	L_θ (mm)	t (mm)	w (mm)	m (g)
1	13.07	1.84	1.99	0.109
2	15.12	1.84	2.00	0.149
3	4.74	1.78	1.98	0.030
4	7.82	1.83	2.01	0.072
5	8.39	1.82	2.01	0.073
6	5.52	1.83	2.01	0.032

Table A.11: Recovered fragments for specimen Ring-Alu-S-11: length (L_θ), thickness (t), width (w) and mass (m).

Fragment	L_θ (mm)	t (mm)	w (mm)	m (g)
1	7.97	1.81	1.96	0.060
2	9.19	1.84	1.97	0.074
3	9.44	1.86	1.97	0.089
4	4.06	1.86	1.98	0.018
5	4.78	1.83	1.97	0.038
6	9.85	1.87	1.98	0.076
7	4.80	1.83	1.96	0.046
8	8.21	1.84	1.98	0.063

Table A.12: Recovered fragments for specimen Ring-Alu-S-12: length (L_θ), thickness (t), width (w) and mass (m).

Fragment	L_θ (mm)	t (mm)	w (mm)	m (g)
1	10.01	1.79	2.01	0.082
2	10.80	1.82	2.00	0.089
3	6.46	1.81	2.01	0.048
4	10.23	1.82	1.98	0.085
5	9.23	1.76	2.00	0.067
6	6.12	1.81	2.00	0.048
7	5.14	1.79	1.99	0.045

Table A.13: Recovered fragments for specimen Ring-Alu-S-13: length (L_θ), thickness (t), width (w) and mass (m).

Fragment	L_θ (mm)	t (mm)	w (mm)	m (g)
1	7.06	1.80	1.97	0.060
2	5.54	1.79	1.95	0.034
3	6.56	1.83	1.99	0.057
4	8.17	1.84	2.00	0.064
5	7.04	1.83	1.98	0.051
6	7.38	1.81	1.99	0.064
7	6.15	1.82	1.95	0.039
8	3.64	1.81	2.00	0.024

Table A.14: Recovered fragments for specimen Ring-Alu-S-14: length (L_θ), thickness (t), width (w) and mass (m).

Fragment	L_θ (mm)	t (mm)	w (mm)	m (g)
1	4.20	1.81	2.01	0.028
2	5.37	1.82	2.01	0.035
3	5.04	1.82	1.99	0.044
4	9.26	1.82	2.01	0.076
5	10.55	1.82	1.99	0.081
6	9.09	1.83	2.02	0.072
7	7.20	1.81	2.02	0.057
8	8.32	1.83	2.01	0.065

Table A.15: Recovered fragments for specimen Ring-Alu-S-15: length (L_θ), thickness (t), width (w) and mass (m).

Fragment	L_θ (mm)	t (mm)	w (mm)	m (g)
1	4.11	1.79	1.99	0.022
2	4.58	1.81	2.00	0.030
3	7.35	1.80	2.00	0.057
4	5.12	1.85	1.98	0.043
5	6.10	1.82	1.99	0.044
6	4.89	1.80	1.98	0.041
7	6.48	1.79	2.01	0.050
8	7.44	1.81	1.97	0.063
9	8.13	1.76	2.00	0.069

Table A.16: Recovered fragments for specimen Ring-Alu-S-16: length (L_θ), thickness (t), width (w) and mass (m).

Fragment	L_θ (mm)	t (mm)	w (mm)	m (g)
1	4.34	1.80	1.97	0.026
2	7.79	1.82	1.97	0.056
3	3.82	1.80	1.96	0.033
4	5.06	1.80	1.98	0.045
5	4.08	1.83	1.97	0.046
6	7.59	1.78	1.98	0.060
7	6.09	1.77	1.98	0.046
8	9.16	1.80	1.99	0.083
9	7.06	1.78	1.98	0.058

Table A.17: Recovered fragments for specimen Ring-Alu-S-17: length (L_θ), thickness (t), width (w) and mass (m).

Fragment	L_θ (mm)	t (mm)	w (mm)	m (g)
1	1.56	1.77	1.99	0.013
2	7.01	1.81	2.00	0.061
3	5.66	1.81	1.99	0.039
4	6.10	1.78	1.99	0.043
5	7.12	1.80	2.00	0.066
6	7.31	1.82	2.00	0.066
7	8.06	1.82	1.97	0.064

Table A.18: Recovered fragments for specimen Ring-Alu-S-18: length (L_θ), thickness (t), width (w) and mass (m).

Fragment	L_θ (mm)	t (mm)	w (mm)	m (g)
1	2.27	1.79	2.01	0.017
2	10.44	1.82	2.01	0.076
3	6.14	1.78	2.01	0.052
4	3.55	1.81	2.00	0.026
5	5.05	1.81	2.02	0.034
6	5.79	1.82	2.02	0.042
7	4.42	1.82	2.04	0.040

Table A.19: Recovered fragments for specimen Ring-Alu-S-20: length (L_θ), thickness (t), width (w) and mass (m).

Fragment	L_θ (mm)	t (mm)	w (mm)	m (g)
1	5.69	1.86	2.03	0.046
2	9.25	1.87	2.03	0.069
3	13.82	1.87	2.01	0.120
4	10.38	1.85	2.01	0.092
5	17.15	1.80	1.99	0.151

Table A.20: Recovered fragments for specimen Ring-Alu-P-1: length (L_θ), thickness (t), width (w) and mass (m).

Fragment	L_θ (mm)	t (mm)	w (mm)	m (g)
1	18.01	1.96	1.91	0.145
2	18.06	1.97	1.85	0.147
3	12.55	1.98	1.85	0.108

Table A.21: Recovered fragments for specimen Ring-Alu-P-2: length (L_θ), thickness (t), width (w) and mass (m).

Fragment	L_θ (mm)	t (mm)	w (mm)	m (g)
1	8.54	1.91	1.88	0.070
2	10.25	1.96	1.87	0.090
3	5.75	1.97	1.89	0.052
4	6.58	1.95	1.87	0.045
5	6.00	1.94	1.90	0.051
6	4.53	1.94	1.87	0.036
7	12.56	1.98	1.85	0.095

Table A.22: Recovered fragments for specimen Ring-Alu-P-3: length (L_θ), thickness (t), width (w) and mass (m).

Fragment	L_θ (mm)	t (mm)	w (mm)	m (g)
1	8.32	1.93	1.86	0.081
2	9.69	1.95	1.89	0.076
3	9.12	1.97	1.86	0.096
4	7.58	1.99	1.85	0.060
5	7.09	1.92	1.88	0.069
6	6.43	1.96	1.83	0.065
7	4.68	1.86	1.85	0.048

Table A.23: Recovered fragments for specimen Ring-Alu-P-4: length (L_θ), thickness (t), width (w) and mass (m).

Fragment	L_θ (mm)	t (mm)	w (mm)	m (g)
1	8.10	1.88	1.86	0.063
2	7.96	1.88	1.88	0.073
3	4.71	1.92	1.84	0.044
4	10.84	1.90	1.88	0.102
5	6.05	1.95	1.86	0.062
6	3.54	1.88	1.87	0.033
7	3.91	1.88	1.86	0.037
8	10.07	1.88	1.87	0.080

Table A.24: Recovered fragments for specimen Ring-Alu-P-5: length (L_θ), thickness (t), width (w) and mass (m).

Fragment	L_θ (mm)	t (mm)	w (mm)	m (g)
1	9.87	1.89	1.83	0.081
2	5.91	1.92	1.81	0.043
3	12.54	1.97	1.82	0.104
4	14.35	1.98	1.90	0.122
5	15.32	1.97	1.85	0.132

Table A.25: Recovered fragments for specimen Ring-Alu-P-6: length (L_θ), thickness (t), width (w) and mass (m).

Fragment	L_θ (mm)	t (mm)	w (mm)	m (g)
1	11.02	1.95	1.90	0.094
2	6.76	2.00	1.84	0.047
3	10.57	1.97	1.90	0.095
4	12.88	1.95	1.88	0.103
5	3.81	1.95	1.94	0.029
6	8.82	1.96	1.85	0.078
7	7.29	1.93	1.86	0.055

Table A.26: Recovered fragments for specimen Ring-Alu-P-7: length (L_θ), thickness (t), width (w) and mass (m).

Fragment	L_θ (mm)	t (mm)	w (mm)	m (g)
1	6.42	1.93	1.94	0.061
2	11.40	1.96	1.89	0.103
3	8.66	1.91	1.89	0.069
4	9.00	1.94	1.87	0.070
5	7.85	1.96	1.93	0.060
6	12.85	1.95	1.86	0.117
7	4.30	1.97	1.92	0.045

Table A.27: Recovered fragments for specimen Ring-Alu-P-8: length (L_θ), thickness (t), width (w) and mass (m).

Fragment	L_θ (mm)	t (mm)	w (mm)	m (g)
1	8.44	1.91	1.89	0.078
2	3.25	1.92	1.93	0.030
3	5.61	1.94	1.95	0.055
4	11.94	1.92	1.93	0.103
5	5.32	1.96	1.91	0.050
6	7.42	1.91	1.93	0.074
7	5.24	1.93	1.92	0.046

Table A.28: Recovered fragments for specimen Ring-Alu-P-10: length (L_θ), thickness (t), width (w) and mass (m).

Fragment	L_θ (mm)	t (mm)	w (mm)	m (g)
1	2.07	1.87	2.26	0.014
2	5.62	1.91	2.16	0.049
3	6.94	1.93	2.23	0.062
4	7.24	1.90	2.19	0.061
5	6.98	1.93	2.21	0.061
6	5.71	1.92	2.21	0.050
7	5.86	1.94	2.19	0.047
8	4.77	1.92	2.21	0.046
9	4.54	1.91	2.19	0.047
10	5.62	1.91	2.19	0.049

Table A.29: Recovered fragments for specimen Ring-Alu-P-11: length (L_θ), thickness (t), width (w) and mass (m).

Fragment	L_θ (mm)	t (mm)	w (mm)	m (g)
1	6.40	1.95	2.13	0.065
2	11.65	1.91	2.13	0.111
3	9.58	1.90	2.13	0.083
4	7.21	1.91	2.15	0.059
5	9.06	1.94	2.15	0.086
6	6.13	1.92	2.13	0.053
7	8.47	1.98	2.17	0.091

Table A.30: Recovered fragments for specimen Ring-Alu-P-12: length (L_θ), thickness (t), width (w) and mass (m).

Fragment	L_θ (mm)	t (mm)	w (mm)	m (g)
1	16.49	1.95	2.17	0.175
2	10.62	1.96	2.18	0.109
3	8.01	1.87	2.20	0.074
4	8.40	1.91	2.17	0.074
5	8.80	1.89	2.18	0.073

Table A.31: Recovered fragments for specimen Ring-Alu-P-13: length (L_θ), thickness (t), width (w) and mass (m).

Fragment	L_θ (mm)	t (mm)	w (mm)	m (g)
1	7.05	1.94	2.19	0.062
2	9.92	1.94	2.16	0.098
3	8.27	1.92	2.19	0.076
4	12.64	1.93	2.18	0.127
5	17.38	1.91	2.16	0.182

Table A.32: Recovered fragments for specimen Ring-Alu-P-15: length (L_θ), thickness (t), width (w) and mass (m).

Fragment	L_θ (mm)	t (mm)	w (mm)	m (g)
1	5.36	1.93	2.17	0.044
2	9.05	1.90	2.14	0.084
3	10.70	1.85	2.15	0.109
4	12.03	1.89	2.17	0.116
5	7.69	1.92	2.15	0.060
6	13.70	1.87	2.17	0.143

Table A.33: Recovered fragments for specimen Ring-Alu-P-16: length (L_θ), thickness (t), width (w) and mass (m).

Fragment	L_θ (mm)	t (mm)	w (mm)	m (g)
1	5.20	1.91	2.22	0.047
2	13.01	1.90	2.19	0.124
3	5.13	1.87	2.18	0.036
4	6.13	1.90	2.24	0.064
5	8.34	1.93	2.22	0.087
6	10.07	1.90	2.20	0.109
7	6.77	1.87	2.18	0.067

Table A.34: Recovered fragments for specimen Ring-Alu-P-17: length (L_θ), thickness (t), width (w) and mass (m).

Fragment	L_θ (mm)	t (mm)	w (mm)	m (g)
1	5.63	1.89	2.11	0.041
2	4.46	1.90	2.14	0.043
3	11.61	1.90	2.17	0.125
4	9.23	1.89	2.16	0.089
5	6.31	1.90	2.14	0.053
6	12.19	1.89	2.14	0.123

Appendix B. Postmortem samples

This section includes post-mortem photography of the recovered fragments corresponding to all *standard* and *performance* specimens tested. Fragments are arranged in a layout that recreates the ring before testing. The drawings on the rings were made before testing for identification of the fragments.

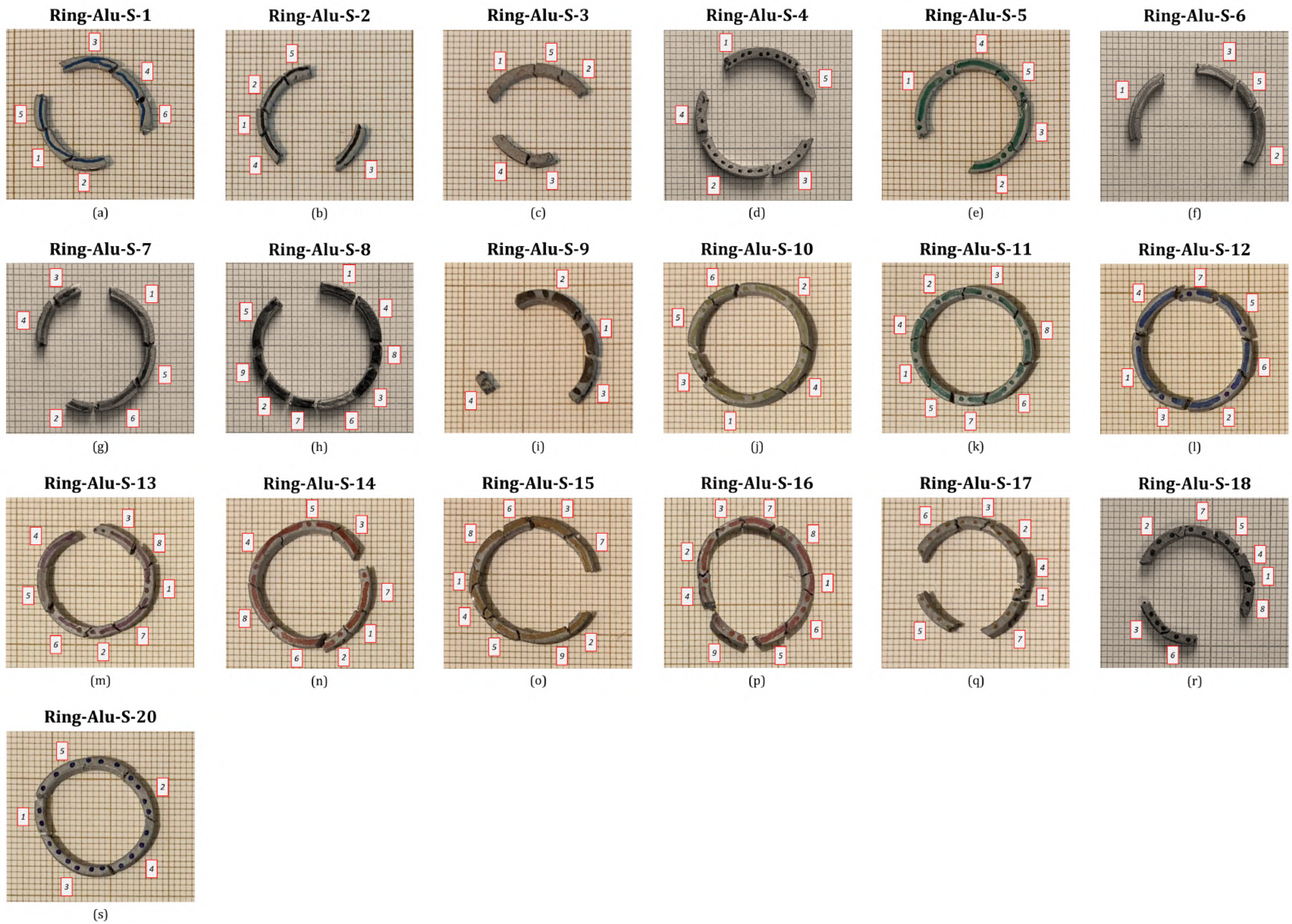

Figure B.16: Post-mortem photography of the recovered fragments corresponding to all *standard* specimens tested. Fragments arranged in a layout that recreates the ring before testing.

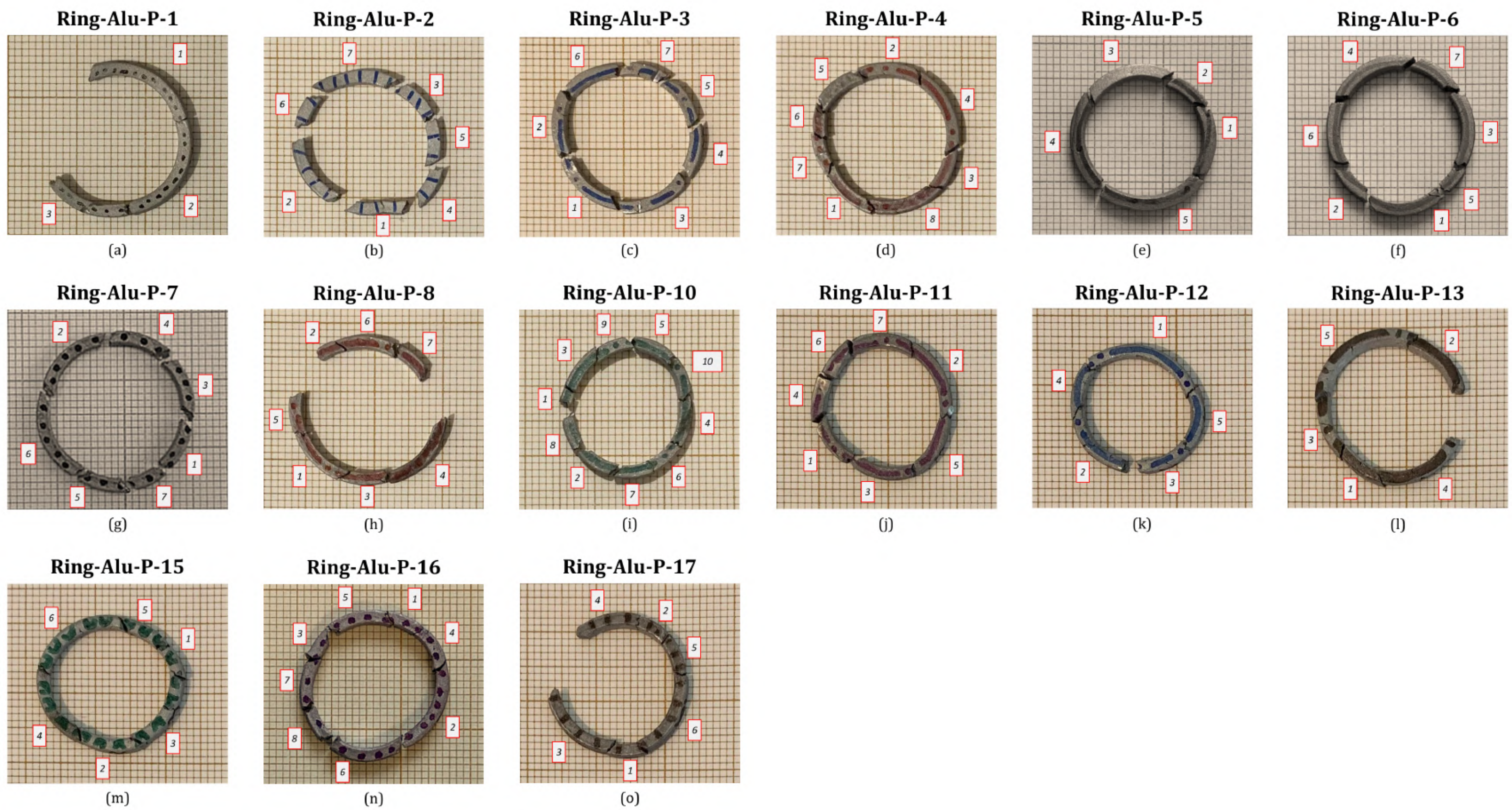

Figure B.17: Post-mortem photography of the recovered fragments corresponding to all *performance* specimens tested. Fragments arranged in a layout that recreates the ring before testing.

References

[1] Altynova, M., Hu, X., Daehn, G.S., 1996. Increased ductility in high velocity electromagnetic ring expansion. Metallurgical and Materials Transactions A 27, 1837–1844.

[2] Cliche, N., Ravi-Chandar, K., 2018. Dynamic strain localization in magnesium alloy AZ31B-O. Mechanics of Materials 116, 189 – 201. IUTAM Symposium on Dynamic Instabilities in Solids.

[3] Fressengeas, C., Molinari, A., 1985. Inertia and thermal effects on the localization of plastic flow. Acta Metallurgica 33, 387–396.

[4] Fyfe, I.M., Rajendran, A.M., 1980. Dynamic pre-strain and inertia effects on the fracture of metals. Journal of the Mechanics and Physics of Solids 28, 17–26.

[5] Gant, F., Seisson, G., Longère, P., El Maï, S., Zinszner, J.L., 2021. Plate-impact-driven ring expansion test (pidret) for dynamic fragmentation, in: DYMAT 2021-13th International Conference on Mechanical and Physical Behaviour of Materaisl Under Dynamic Loading-Madrid (Spain)-Sept. 19-24, 2021.

[6] Grady, D.E., Benson, D.A., 1983. Fragmentation of metal rings by electromagnetic loading. Experimental Mechanics 12, 393–400.

[7] Grady, D.E., Kipp, M.E., Benson, D.A., 1984. Energy and statistical effects in the dynamic fragmentation of metal rings, in: Harding, J. (Ed.), Mechanical properties at high strain rates, Institute of Physics, Bristol. pp. 315–320.

[8] Grady, D.E., Olsen, M.L., 2003. A statistics and energy based theory of dynamic fragmentation. International Journal of Impact Engineering 29, 293–306.

[9] Janiszewski, J., 2012. Ductility of selected metals under electromagnetic ring test loading conditions. International Journal of Solids and Structures 49, 1001–1008.

[10] Jones, D.R., Chapman, D.J., Eakins, D.E., 2013. A gas gun based technique for studying the role of temperature in dynamic fracture and fragmentation. Journal of Applied Physics 114, 173508.

[11] Kahana, E., Ben-Artzy, A., Sadot, O., Shneck, R.Z., 2015. Microstructural evolution of AZ31 magnesium alloy after high strain rate expanding rings tests. Materials Science and Engineering: A 641, 274–280.

[12] Kipp, M.E., Grady, D.E., 1985. Dynamic fracture growth and interaction in one dimension. Journal of the Mechanics and Physics of Solids 33, 399–415.

[13] Kristoffersen, M., Costas, M., Koenis, T., Brøtan, V., Paulsen, C.O., Børvik, T., 2020. On the ballistic perforation resistance of additive manufactured AlSi10Mg aluminium plates. International Journal of Impact Engineering 137, 103476.

[14] Ma, H., Mao, W., Su, H., Zhu, H., Cui, X., Huang, L., Li, J., Wu, M., 2021. Rate-related study on mechanical properties and fracture characteristics in aluminium alloy via electromagnetic ring expansion test. International Journal of Mechanical Sciences 209, 106712.

[15] Materialise, 2022. Materialise NV, Belgium.

[16] Mercier, S., Molinari, A., 2003. Predictions of bifurcations and instabilities during dynamic extensions. International Journal of Solids and Structures 40, 1995–2016.

[17] Mercier, S., Molinari, A., 2004. Analysis of multiple necking in rings under rapid radial expansion. International Journal of Impact Engineering 30, 403–419.

[18] Mott, N.F., 1947. Fragmentation of shell cases. Proceedings of the Royal Society of London. Series A. Mathematical and Physical Sciences 189, 300–308.

[19] Nieto-Fuentes, J.C., Espinoza, J., Sket, F., Rodríguez-Martínez, J.A., 2022. High-velocity impact fragmentation of additively-manufactured metallic tubes. Submitted for Publication doi:10.31224/2627.

[20] Niordson, F.L., 1965. A unit for testing materials at high strain rates. Experimental Mechanics 5, 29–32.

[21] Pardoen, T., Hutchinson, J., 2003. Micromechanics-based model for trends in toughness of ductile metals. Acta Materialia 51, 133–148.

[22] Rajendran, A.M., Fyfe, I.M., 1982. Inertia effects on the ductile failure of thin rings. Journal of Applied Mechanics 49, 31–36.

[23] Soni, H., Limbasiya, N., Jain, A., Gill, S.S., Sahlot, P., 2022. Investigation of mechanical and surface properties of additively manufactured AlSi10Mg part produced through direct metal laser sintering. Materials Today: Proceedings 62, 7204–7209. International Conference on Additive Manufacturing and Advanced Materials (AM2).

[24] Stepanov, G.V., Babutskii, A.I., 1984. Experimental study of the fragmentation of metal rings. Strength of Materials 16, 1199–1202.

[25] Thomason, P., 1970. A theoretical estimate of the surface energy in ductile fracture. International Journal of Fracture Mechanics 6, 353–356.

[26] Vogler, T.J., Thornhill, T.F., Reinhart, W.D., Chhabildas, L.C., Grady, D.E., Wilson, L.T., Hurricane, O.A., Sunwoo, A., 2003. Fragmentation of materials in expanding tube experiments. International Journal of Impact Engineering 29, 735–746.

[27] Weavwe, J., Rosenthal, I., 2021. Understanding anisotropic tensile properties of laser powder bed fusion additive metals: A detailed review of select examples. Advanced Manufacturing Series (NIST AMS) , 100–44.

[28] Winter, R.E., Prestidge, H.G., 1978. A technique for the measurement of the high strain rate ductility of metals. Journal of Materials Science 13, 1835–1837.

[29] Wood, P., Rusinek, A., Platek, P., Janiszewski, J., Sienkiewicz, J., Gunputh, U.F., Rajkowski, K., Miguélez, M.H., 2021. High strain rate effect on tensile ductility and fracture of AM fabricated Inconel 718 with voided microstructures. Materials & Design 208, 109908.

[30] Zhang, H., Ravi-Chandar, K., 2006. On the dynamics of necking and fragmentation - I. Real-time and post-mortem observations in Al 6061-O. International Journal of Fracture 142, 183–217.

[31] Zhang, H., Ravi-Chandar, K., 2008. On the dynamics of necking and fragmentation - II. Effect of material properties geometrical constraints and absolute size. International Journal of Fracture 150, 3–36.

[32] Zhou, F., Molinari, J.F., Ramesh, K.T., 2006. An elasto-visco-plastic analysis of ductile expanding ring. International Journal of Impact Engineering 33, 880–891.